

[Click here to view linked References](#)

1 **RAINFALL THRESHOLD FOR INITIATING EFFECTIVE**  
2  
3 **STRESS DECREASE AND FAILURE IN WEATHERED**  
4  
5 **TEPHRA SLOPES**  
6  
7

8  
9 **Max Oke Kluger<sup>1\*</sup>, M. Ehsan Jorat<sup>2</sup>, Vicki G. Moon<sup>3</sup>, Stefan Kreiter<sup>4</sup>, Willem de**  
10 **Lange<sup>5</sup>, Tobias Mörz<sup>6</sup>, Thomas Robertson<sup>7</sup>, David J. Lowe<sup>8</sup>**  
11  
12  
13

14  
15 <sup>1</sup>MARUM – Research Faculty, University of Bremen, Leobener Straße 8, 28359 Bremen,  
16 Germany, Orcid:0000-0001-9130-8948  
17

18  
19 <sup>2</sup>School of Applied Sciences, Abertay University, Dundee, DD11HG, United Kingdom, Or-  
20 cid: 0000-0001-6972-5921  
21

22  
23 <sup>3</sup>School of Science, University of Waikato, Hamilton, New Zealand, Orcid:0000-0001-7378-  
24 8490  
25

26  
27 <sup>4</sup>MARUM – Research Faculty, University of Bremen, Leobener Straße 8, 28359 Bremen,  
28 Germany, Orcid:0000-0002-1110-7765  
29

30  
31 <sup>5</sup>School of Science, University of Waikato, Hamilton, New Zealand, Orcid: 0000-0002-6467-  
32 0308  
33

34  
35  
36 <sup>6</sup>MARUM – Research Faculty, University of Bremen, Leobener Straße 8, 28359 Bremen,  
37 Germany, Orcid:0000-0002-6865-7864  
38

39  
40 <sup>7</sup>School of Science, University of Waikato, Hamilton, New Zealand  
41

42  
43 <sup>8</sup>School of Science, University of Waikato, Hamilton, New Zealand, Orcid: 0000-0002-2547-  
44 6019  
45

46  
47 \*Corresponding author, Email: [mkluger@marum.de](mailto:mkluger@marum.de)  
48  
49

50  
51  
52 *Citation:*

53 Kluger, M.O., Jorat, M.E., Moon, V.G., Kreiter, S., de Lange, W.P., Mörz, T., Robertson, T., Lowe, D.J.  
54 2020. Rainfall threshold for initiating effective stress decrease and failure in weathered tephra slopes.  
55 *Landslides* DOI: 10.1007/s10346-019-01289-2 (online from 19 October 2019)  
56  
57  
58  
59  
60  
61  
62  
63  
64  
65

1 **Abstract**

2 Rainfall is one of the most important triggers of slope failure. Weathered pyroclastic (tephra)  
3 deposits are especially vulnerable to slope failure because they commonly form slopes of high  
4 porosity and high clay content. Empirically-derived thresholds for the triggering of landslides  
5 are commonly based on rainfall conditions and have been widely applied in volcanic soils.  
6 However, so far only few researchers utilized pore water pressure in the slope as additional  
7 variable for the threshold calibration. Here we derived a new rainfall threshold for initiating the  
8 decrease in effective stress in the slope by analyzing a long-term record of rainfall and piezom-  
9 eter data from a slide-prone coastal area in northern New Zealand that consists of clayey, hal-  
10 loysitic tephra deposits. The level of effective stress decrease increases with rainfall intensity  
11 and duration. We observed highest effective stress decrease of up to 36 % during rainfall events  
12 that triggered landslides in our study area. The effective stress threshold exhibits a satisfactory  
13 predictive capability. The probability of correctly predicting a decrease in effective stress is  
14 53 %. The effective stress threshold contributes towards the implementation of the decrease in  
15 effective stress into rainfall thresholds for the occurrence of landslides.

16  
17  
18 **Keywords** landslides; rainfall threshold; effective stress; weathered tephra; spheroidal hal-  
19 loysite; rainfall-induced slope failure

## 1. INTRODUCTION

Rainfall-induced landslides occur globally in all types of environments, posing a major natural hazard to people and infrastructure. Coastal environments are especially vulnerable to landslides because they often consist of highly populated terrain with steep slopes (Agostini et al., 2014; Assier-Rzadkiewicz et al., 2000; Longva et al., 2003; Rösner, 2016). The severity of landslides is further controlled by the presence of sensitive soils in the slope. The special role of sensitive soils is their pronounced post-failure softening behavior, which may lead to progressive landslides with long runout distance that are difficult to predict (Demers et al., 2014; Kvalstad et al., 2005; L'Heureux et al., 2014). Tephra deposits, encompassing all pyroclastic materials of any grain size (Lowe, 2011), are highly susceptible to slope failure and have been responsible for catastrophic landslides (Chigira, 2014; Sidle and Ochiai, 2006). Halloysite is a common weathering product of rhyolitic (silica-rich) tephra (Churchman and Lowe, 2012) and has been found to dominate slide surfaces of rainfall-induced landslides in Hong Kong, Japan, New Zealand, Hawaii, and the conterminous United States (Chigira, 2014; Chigira and Yokoyama, 2005; Irfan, 1992, 1998; Kirk et al., 1997; Kluger et al., 2017; Parry et al., 2000, 2001; Shaller et al., 2016; Taskey, 1977; Wen and Aydin, 2003; Yamao et al., 2016). Halloysite is known to form low-permeability soils with high sensitivity (Kluger et al., 2017; Moon et al., 2015b; Smalley et al., 1980). A Review by Chigira (2014), for example, highlighted the importance of better understanding the trigger mechanisms and landslides dimensions in halloysitic soils.

Reduction of effective stress due to rainfall-induced excess pore water pressure is a significant trigger of landslides (Cruden and Varnes, 1996). Rainfall thresholds are widely used to forecast the likely occurrence of landsliding by defining the minimum rainfall necessary to trigger landslides (Segoni et al., 2018a). Caine (1980) developed a first global rainfall threshold, which links rainfall intensity and duration to the occurrence of landslides. Since then, a large variety of rainfall thresholds have been derived at different scales (global, regional, local), by using different rainfall parameters (rainfall intensity, duration, antecedent precipitation), and for various types of landslides (Guzzetti et al., 2007, 2008; Segoni et al., 2018a). In their recent review, Segoni et al. (2018a) summarized that most rainfall thresholds were derived for shallow landslides and debris flows, whereas only few rainfall thresholds for deep-seated landslides, rockslides, and earthflows had been studied. Furthermore, Segoni et al. (2018a) recognized that most studies solely rely on rainfall data when calibrating rainfall thresholds. They found only two case studies – Baum and Godt (2010) and Napolitano et al. (2016) – in which pore water pressure data provided additional insight into the trigger mechanism of landslides. Understanding changes in pore water pressure due to rainfall is needed to calculate changes in effective stress in the soil slope (Duncan et al., 2014) and its evaluation would therefore offer a new beneficial perspective in the determination of rainfall thresholds (Segoni et al., 2018a).

### 1.1 Suitability of study area

57 Our study area is the Omokoroa Peninsula ('Omokoroa' hereafter), located in the central part of Tau-  
1 58 ranga Harbour, New Zealand's largest barrier-enclosed estuarine lagoon (Fig. 1A-B). Omokoroa's ge-  
2 59 ology consists mainly of a thick succession of Quaternary-aged rhyolitic tephra-fall deposits derived  
3 60 largely from eruptions in the Taupo Volcanic Zone, together with intercalated paleosols, underlain by  
4 61 ignimbrite (Briggs et al., 2005). One specific composite unit within the siliceous tephra succession, the  
5 62 Pahoia Tephra sequence ('Pahoia Tephra' hereafter), has been highly weathered to form clay-rich de-  
6 63 posits dominated by halloysite and has very high sensitivities (Kluger et al., 2017; Smalley et al., 1980).  
7 64 These highly sensitive Pahoia Tephra were involved in the deep-seated Bramley Drive landslide, lo-  
8 65 cated on the northwest coast of Omokoroa (Kluger et al., 2017; Moon et al., 2015b). The main failure  
9 66 occurred in 1979 after prolonged heavy rainfall and was reactivated by smaller retrogressive failures in  
10 67 2011, and 2012. The Pahoia Tephra, acting as an aquiclude as well as sliding material, were transported  
11 68 over long runout distances into Tauranga Harbour. During two rainfall events associated with cyclones  
12 69 Debbie and Cook in 2017, 27 new landslides occurred along the coast of Omokoroa causing damage to  
13 70 numerous houses and properties (Tab. 1C-E). This study area is therefore ideal for investigating trigger  
14 71 mechanisms and landslide dimensions of rainfall-induced landslides in sensitive halloysitic tephra, and  
15 72 demonstrably important also for informing landslide hazard analysis and potential mitigation (Basher,  
16 73 2013; Crozier, 2005).

## 74 75 **1.2 Outline of our approach**

76 In this study, we used field observations including mapping of landslides, and a combination of bathym-  
77 etry and seismic data, to identify the failure dimensions and geological preconditioning factors of the  
78 landslides at Omokoroa. We then compare these features with those of landslides in various material  
79 types and environments worldwide. By analyzing 4.5 years of rainfall and pore water pressure data  
80 recorded at the Bramley Drive landslide since 2014, we calibrated and validated empirical rainfall  
81 thresholds for the occurrence of landslides and for the initiation of effective stress decrease in the slope.

## 82 83 **2. GEOLOGICAL SETTING**

84 The Tauranga basin extends along the Bay of Plenty coastline on the northeastern part of New Zealand's  
85 North Island (Briggs et al., 1996) (Fig. 1B). The Waiteariki Ignimbrite, deposited c. 2.09 Ma (Briggs et  
86 al., 2005), forms the local basement. Its eruption initiated a period of rapid subsidence (Houghton and  
87 Cuthbertson, 1989). The ensuing basin was infilled in part by volcanogenic sediments, ignimbrites, and  
88 silica-rich tephra-fall deposits originating from eruptions in the Coromandel Volcanic Zone and the  
89 Taupo Volcanic Zone. The post-glacial marine transgression after the Last Glacial Maximum (attaining  
90 near-modern sea level c. 7,500 years ago) formed a large barrier-enclosed mesotidal estuarine lagoon,  
91 the Tauranga Harbour (Briggs et al., 1996). The lagoon is blocked from the sea by two tombolos at  
92 Bowentown and Mt Maunganui, and the Pleistocene and Holocene barrier island of Matakana Island  
93 (Shepherd et al., 2000). Most of the lagoon comprises extensive estuaries and mudflats. A number of

94 terraces extend into Tauranga Harbour as northeast- to north-northeast-trending peninsulas, which com-  
95 monly have near-level surfaces 20 to 40 m above sea level and steep slopes or cliffs on their coasts that  
96 are prone to landsliding (Briggs et al., 1996; Chappell, 1975).

97  
98 One of these peninsulas is that at Omokoroa (Fig. 1A), which has experienced numerous coastal land-  
99 slides (Fig. 1C-E). Omokoroa stratigraphically comprises a ~40-m-thick succession of mainly Quater-  
100 nary rhyolitic tephra (Fig. 2A): the Pahoia Tephra sequence includes (from base to top) lignite, paleosol  
101 P1, nonwelded pumiceous deposits of the Te Puna Ignimbrite (c. 0.93 Ma), and a series of weathered  
102 clay-rich halloysitic tephra beds, which are divided into lower and upper Pahoia Tephra based on  
103 a distinct paleosol (P2). All of these deposits and intercalated paleosols are overlain by successions of  
104 younger, strongly-weathered tephra called Hamilton Ashes (c. 0.35 to c. 0.05 Ma) and late Quaternary  
105 tephra ( $\leq$  c. 0.05 Ma). Apart from the near-surface late Quaternary tephra (which are mainly allo-  
106 phanic), the tephra have been weathered to halloysites with different morphologies, ranging from  
107 mainly tubular in the Hamilton Ashes and Upper Pahoia Tephra, to mainly spheroids in the lower Pa-  
108 hoia Tephra, and to mainly polyhedrons and books in the Te Puna Ignimbrite (Cunningham et al., 2016;  
109 Kluger et al., 2017). The lower Pahoia Tephra include the highly sensitive halloysitic layer that was  
110 involved in the failure of the 1979 Bramley Drive landslide (Fig. 2B-C). Kluger et al. (2017) reported a  
111 new mushroom cap-shaped variety of the spheroidal halloysite morphology (Fig. 2D), which, through  
112 its surface-charge characteristics, causes the layer to be highly sensitive and thus contributes to the land-  
113 slide susceptibility at Omokoroa. The highly sensitive halloysitic layer is porous (Smalley et al., 1980),  
114 but has also low permeability (Moon et al., 2015b), affecting the hydrogeology of the tephra successions  
115 at Omokoroa. Based on piezometer recordings at the Bramley Drive landslide, an aquiclude located in  
116 the lower Pahoia Tephra prohibits downward directed drainage of rainwater, whereas an overlying  
117 aquifer is directly connected to the surface and allows rain induced effective stress fluctuations in the  
118 slope (Moon et al., 2015a).

### 119 120 **3. MATERIALS AND METHODS**

#### 121 **3.1. Landslide characterization**

122 The landslides that occurred at Omokoroa's coast since the 1979 Bramley Drive landslide were charac-  
123 terized according to material composition, type, volume, and travel angle. We performed a detailed  
124 mapping survey of landslide after the 2017 cyclone season in April 2017. The mapping of landslides  
125 included the following steps. The lithological compositions of the slides were identified by descriptions  
126 of samples taken from the landslide scarp and slide debris, or alternatively through observation of ex-  
127 posed scarp faces and correlations to the known regional stratigraphy at Omokoroa. The landslides were  
128 classified according to Cruden and Varnes (1996), being either deep-seated (with rotational slip surface),  
129 shallow, or composite earth slides. The composite earth slides always resulted from both deep-seated  
130 and shallow failures and are hereafter attributed either to the deep-seated or shallow earth slides on the

131 basis of the dominant mode of failure. The decision about which mode of failure dominated the landslide  
 132 was made by the authors' expert knowledge. We calculated volumes of deep-seated landslides  $V_{ds}$  by  
 133 assuming the slip surfaces followed the shape of half an ellipsoid with semiaxes  $D_s$ ,  $W_s/2$ , and  $L_s$  (Eq. 1,  
 134 Cruden and Varnes, 1996).

$$135$$

$$136 \quad V_{ds} = \frac{1}{6} \pi D_s \cdot W_s \cdot L_s \quad (1)$$

137

138 where  $L_s$  is the distance from toe of slip surface to crown of the main scarp.  $W_s$  is the maximum width  
 139 between flanks of the landslide perpendicular to  $L_s$ .  $D_s$  is the maximum depth of the slip surface below  
 140 original ground surface, measured perpendicular to the plane containing  $W_s$  and  $L_s$ . The orientation of  
 141 the original ground surface was derived from a 1-m-resolution LIDAR digital elevation model of Omo-  
 142 koroa, which was recorded before the landslides in 2015. It is accepted practice to estimate volumes of  
 143 shallow landslides  $V_s$  (Eq. 2) from landslide area  $A_L$  (Eq. 3) and two empirically derived parameters,  
 144 namely the scaling exponent  $c$  and intercept  $a$  (Guzzetti et al., 2009; Larsen et al., 2010; Malamud et  
 145 al., 2004).

$$146$$

$$147 \quad V_s = a A_L^c \quad (2)$$

$$148 \quad A_L = W_s \cdot L_s \quad (3)$$

149

150 In our study, we used a scaling exponent of  $c = 1.332$  and an intercept of  $\log(a) = -0.836$  to estimate  
 151 volumes of shallow landslides. These values are derived from an international database of soil landslides  
 152 (Larsen et al., 2010). The travel angle  $\beta$  of landslides is calculated following Cruden and Varnes (1996)  
 153 using Eqs. 4 and 5.

$$154$$

$$155 \quad \tan(\beta) = H/L \quad (4)$$

$$156 \quad \beta = \tan^{-1} \left( \frac{H}{L} \right) \quad (5)$$

157

158 where  $H/L$  is the height-to-length ratio (Cruden and Varnes, 1996), which is calculated from the vertical  
 159  $H$  and horizontal distances  $L$  between crown and tip of the landslide deposits, respectively. The volume  
 160 and travel angle of the 1979 Bramley Drive landslide were estimated from Gulliver and Houghton  
 161 (1980).

162

163 We further studied the volumes and travel angles of historical landslides that occurred at Omokoroa by  
 164 surveying the geological record of the sediments deposited in the subtidal area close to Omokoroa's  
 165 coast. By using a 200/400kHz shallow water multibeam echosounder (Reson Seabat 7125) onboard  
 166 vessel *Pandora*, and a 3.5kHz seismic system (Knudsen Pinger CHIRP SBP) mounted on vessel *Tai*

167 *Rangahau*, we mapped the seafloor morphology and sedimentary subsurface structures of potential rem-  
168 nant landslide deposits. The bathymetric and seismic data cover an elongated northeast-trending area  
169 c. 1,300 m long and c. 250 m wide (Fig. 1A). The bathymetric data have a grid resolution of 1 m by 1 m  
170 and the seismic data form a grid of approximately parallel profiles with c. 50 m spacing.

171

### 172 **3.2. Evaluation of rainfall and pore water pressure**

173 We consider our study area at Omokoroa to be of local scale, with maximal length of 1,800 m, maximal  
174 width of 300 m, and an area of c. 0.5 km<sup>2</sup>. Rainfall that occurred from January 2014 to June 2018 was  
175 therefore recorded by a single tipping bucket rain gauge (Ogawa Seiki Co.) located close to the Bramley  
176 Drive landslide (Fig. 1A) (Moon et al., 2015a). According to Segoni et al. (2018a), a rain gauge density  
177 of 200 per 100 km<sup>2</sup>, as used in our study, is within the middle range considered in recent studies about  
178 rainfall thresholds. The maximal distance between the rain gauge and landslides was c. 1000 m. The rain  
179 gauge at the Bramley Drive landslide exhibited time periods with data gaps (Fig. 3B). We therefore  
180 supplemented the missing record with rainfall data collected from the nearest available rain gauge at  
181 Goodall Road, Whakamarama, being located c. 6.5 km SW of Omokoroa (Fig. 1B). Because rainfall  
182 within Tauranga Harbour has been observed to be variable (Quayle, 1984), we confirmed the accordance  
183 between both rainfall regimes by statistical correlation (Fig. 3C-D). For this purpose, we identified rain-  
184 fall events that were recorded by both rain gauges and found that cumulated rainfall and rainfall duration  
185 at the Bramley Drive landslide are both well represented by the rain gauge at Goodall Road, Whaka-  
186 marama. The sampling rates for the rainfall gauges were every 10 minutes at the Bramley Drive land-  
187 slide and every 60 minutes at Goodall Road, Whakamarama. Because of that difference, we resampled  
188 the rainfall data of both stations to hourly rainfall.

189

190 Pore water pressure changes were recorded every 10 minutes from January 2014 to June 2018 by three  
191 piezometers (Glötzl PP-3). The piezometers have been installed in a borehole close to the rain gauge of  
192 the Bramley Drive landslide at depths of 12, 21, and 27.5 m (Moon et al., 2015a). The depths were  
193 chosen to record the pore water pressure in the aquifer (above and below the mean ground water level)  
194 and in the confined aquifer below the aquiclude and are hereafter referred to as upper, middle, and lower  
195 piezometers, respectively (Fig. 2C). Because of technical issues, the piezometers did not record any data  
196 from March to July 2016 (indicated by ‘data gap’ in Fig. 3A).

197

198 We analyzed the rainfall and piezometer data to relate rainfall parameters (cumulated rainfall, rainfall  
199 intensity, and duration) of individual rainfall events to pore water pressure increase and to the triggering  
200 of landslides. The extraction of rainfall parameters from the rainfall data and the separation of individual  
201 rainfall events was based on defining a standard time period without rainfall. The duration of dry periods  
202 commonly chosen for separating individual rainfall events varies from six hours (Tiranti and Rabuffetti,  
203 2010) to four days (Brunetti et al., 2010). In our study, the pore water pressure from rainfall dissipated

204 within a few hours after the rainfall stopped and never exceeded six hours (Fig. 3E). Therefore, we  
 1 205 defined an individual rainfall event as continuous rainfall being separated from the next rainfall event  
 2 206 by a dry period of at least six hours (following the suggestions made by Tiranti and Rabuffetti, 2010).  
 3 207 For each rainfall event, we calculated the cumulated rainfall, duration, and rainfall intensity. We classi-  
 4 208 fied the rainfall events that caused an increase in pore water pressure in at least one of the piezometers  
 5 209 as ‘large rainfall events’, and those with no impact on the pore water pressure as ‘small rainfall events.’  
 6 210 Destabilization of the soil slope because of large rainfall events was assessed by considering the decrease  
 7 211 in effective stress due to pore water pressure. The effective stress  $\sigma'$  was calculated using Eq. 6.

$$13 \text{ 212} \quad \sigma' = \sigma - u \quad (6)$$

14 214  
 15 215 where  $\sigma$  is the total overburden stress, which we estimated from long-spaced gamma density logging in  
 16 216 the slope of the Bramley Drive landslide (Kluger et al., 2018), and  $u$  is the pore water pressure measured  
 17 217 by the piezometers.

18 218  
 19 219 All 27 landslides since January 2014 were observed shortly after two large rainfall events during cy-  
 20 220 clones Debbie and Cook in 2017. The timings of these landslides were solely based on eye witness  
 21 221 reports of residents living close to the coast of Omokoroa, yielding a temporal resolution of landslide  
 22 222 occurrence of about one day. The attribution of rainfall events to the triggering of landslides was there-  
 23 223 fore performed manually, without any measurement of soil displacement during landslides. Because of  
 24 224 the low number of rainfall events ( $N = 2$ ) that triggered landslides, we did not derive own rainfall  
 25 225 thresholds for the occurrence of landslides, but compared the two large rainfall events during cyclones  
 26 226 Debbie and Cook that triggered landslides at Omokoroa to the global rainfall intensity-duration thresh-  
 27 227 old suggested by Caine (1980), which was later updated by Sidle and Ochiai (2006) (Eq. 7).

$$28 \text{ 228} \quad I = \alpha D^{-\gamma} \quad (7)$$

29 230  
 30 231 where  $I$  is the rainfall intensity (mm/h),  $D$  is the duration of rainfall (h), and  $\alpha = 13.58$  and  $\gamma = 0.38$   
 31 232 are the intercept and slope of the power law function, respectively. Additionally, we adopted the Fre-  
 32 233 quentist method to statistically analyze rainfall events that caused an effective stress decrease (i.e. large  
 33 234 rainfall events) and calibrated a rainfall intensity-duration threshold for the beginning of effective stress  
 34 235 decrease. The Frequentist method was first described by Brunetti et al. (2010) and has since been applied  
 35 236 in several study areas in Italy (Peruccacci et al., 2012; Segoni et al., 2018a). Following Brunetti et al.  
 36 237 (2010), we applied frequency analysis on the large rainfall events and calibrated a rainfall threshold  
 37 238 (Eq. 7) for the beginning of effective stress decrease at the 5 % confidence interval. Assuming the cata-  
 38 239 logue of large rainfall events sufficiently represents the rainfall conditions at Omokoroa, we can state

240 that the probability of effective stress decrease by rainfall below this threshold is less than 5 % (Brunetti  
241 et al., 2010).

242  
243 We validated the predictive capability of the global rainfall threshold of Sidle and Ochiai (2006) and  
244 our new effective stress threshold by compiling contingency matrices (one for each threshold) that clas-  
245 sify rainfall events as either true positives (*TP*), true negatives (*TN*), false positives (*FP*), or false neg-  
246 atives (*FN*) (Tab. 2). The validation was performed using the entire data set of rainfall events between  
247 January 2014 and June 2018. The contingency matrices were used to calculate different skill scores  
248 (sensitivity, specificity, positive prediction power, negative prediction power), all of which are common  
249 statistical parameters to evaluate predictive capability (Martelloni et al., 2012; Rosi et al., 2015; Segoni  
250 et al., 2018a).

## 251 252 **4. COASTAL LANDSLIDES IN HALLOYSITIC TEPHRA DEPOSITS**

### 253 **4.1. Preconditioning factors**

254 Many landslides occurred along the northwest coast of Omokoroa as a consequence of two large rainfall  
255 events during cyclones Debbie and Cook in 2017. We counted a total of 27 coastal landslides and over-  
256 laid the topography in Fig. 1A with our mapping results of main scarps and dimensions of landslide  
257 deposits. The landslides have an average spacing distance of 80 m between one another and affected the  
258 highly populated coastal residential area of Omokoroa (Fig. 1C-E). The majority of landslides resulted  
259 from shallow slope-parallel failures within the upper unwelded pumiceous deposits of the Te Puna Ig-  
260 nimbrite and overlying halloysitic tephra deposits of the Pahoia Tephra (c.f. Fig. 1C, Table 1). Shallow  
261 landslides occur occasionally along the entire coastline and become dominant at the eastern coast along  
262 Myrtle Drive and Crapp Reserve (Fig. 1A).

263  
264 We counted ten landslides that were deep-seated. One of these, the McDonnell Street landslide (L-9),  
265 followed a failure and sliding mechanism similar to that of the 1979 Bramley Drive landslide (L-11).  
266 Both landslides, depicted in Figs. 1D-E, resulted from an initial rotational failure that reached into the  
267 highly sensitive lower Pahoia Tephra. The landslide masses then eroded the upper parts of the Te Puna  
268 Ignimbrite until they reached sea level and formed flow slides into the lagoon of Tauranga Harbour  
269 (Gulliver and Houghton, 1980). The benches of the initial rotational failures are highlighted by white  
270 dashed lines in Figs. 1D-E. The other deep-seated landslides resulted from rotational failures, which  
271 were sometimes associated with minor shallow slides.

272  
273 Preconditioning factors for landslides have been widely discussed in the literature (Cruden and Varnes,  
274 1996; Duncan et al., 2014; Varnes, 1978). We consider that the most important preconditioning factors  
275 for the coastal landslides at Omokoroa lie in a combination of toe erosion, low permeability, being in  
276 the order of  $5 \cdot 10^{-10}$  m/s, and high sensitivity of the halloysitic tephra layers within the lower Pahoia

277 Tephra (Kluger et al., 2018; Kluger et al., 2017; Moon et al., 2015b). Low-permeability clay layers  
278 interbedded in soil slopes can occur in all types of deposits and environments worldwide and these  
279 situations probably represent the most intensely studied preconditioning factor for pore water pressure-  
280 induced landslides (Zaruba and Mencl, 2014). Regardless of the clay layers' mineralogy, their low-  
281 permeability reduced water infiltration into the slope, therefore increased pore water pressure in the  
282 overlying aquifer. Following the effective stress principle (Eq. 3) and the Mohr-Coulomb failure crite-  
283 rion, an increase in pore water pressure causes a reduction in effective stress, and consequently a reduc-  
284 tion in shear strength (Labuz and Zang, 2012). Where pore water pressure reduces the shear strength of  
285 the slope material to the critical level, landslides are triggered.

286  
287 Sensitivity is the ratio of maximum shear strength to post-failure residual shear strength, where a value  
288 of more than 30 is defined as highly sensitive (Norsk Geoteknisk Forening, 1974; Skempton and  
289 Northey, 1952). Kluger et al. (2017) studied the relationship between halloysite clay morphology and  
290 sensitivity in intact tephra from the Bramley Drive landslide and measured the highest sensitivities of  
291  $S = 55$  in mushroom cap-shaped spheroidal halloysite, whereas sensitivity development was lower ( $S \leq$   
292 10) in tubular halloysite. The mushroom cap-shaped spheroidal halloysite is most abundant in the lower  
293 Pahoia Tephra, which have been involved in the failure of the 1979 Bramley Drive landslide (Figs. 1E  
294 and 2). Our observations of the compositions of the slide material show that 30% of the deep-seated  
295 landslides initially failed within the lower Pahoia Tephra (Table 1). Furthermore, a two-third of shal-  
296 low-translational landslides also involved failure within the Pahoia Tephra. These observations high-  
297 light the special role of spheroidal halloysite in landslides at Omokoroa. Similar observations have also  
298 been reported in Japan, where 'ball-shaped' halloysite was associated with slip surfaces in weathered  
299 tephra (Tanaka, 1992).

300  
301 Spheroidal halloysite is commonly formed by rapid precipitation from silicon-rich and aluminum-bear-  
302 ing solutions derived from the dissolution of volcanic glass shards and primary mineral grains (Cravero  
303 and Churchman, 2016; Joussein et al., 2005). Researchers have reported the occurrence of spheroidal  
304 halloysites in cold to tropical regions around the world within various volcanogenic host materials of  
305 rhyolitic, andesitic, and basaltic composition (Adamo et al., 2001; Askenasy et al., 1973; Birrell et al.,  
306 1955; De Oliveira et al., 2007; Jeong and Kim, 1996; Kirkman, 1977; Loughnan and Roberts, 1981;  
307 Parham, 1970; Quantin and Rambaud, 1987; Romero et al., 1992; Saigusa et al., 1978; Sieffermann and  
308 Millot, 1969; Singer et al., 2004; Wada and Kakuto, 1985). Furthermore, neoformation of spheroidal  
309 halloysite was also observed in tephra layers offshore from Sumatra and Peru (Imbert and Desprairies,  
310 1987; Pouclet et al., 1990). This global occurrence shows the importance of better understanding the  
311 role of spheroidal halloysite in sensitivity development and its role in preconditioning large landslides  
312 with a progressive failure mechanism.

313

## 314 4.2. Landslide dimensions

1 315 We evaluated the dimensions of the landslides that have occurred along the coast of Omokoroa since  
2 316 1979 (Fig. 4). The majority of landslides are of relatively small volumes, ranging between ~100 and  
3 317 4,500m<sup>3</sup>, and steep travel angles between 17° and 60° (Table 1). Notable exceptions are the McDonnell  
4 318 Street landslide (L-9) and the 1979 Bramley Drive landslide (L-11), having volumes of c. 11,000 and  
5 319 60,000m<sup>3</sup> and travel angles of 15° and 9°, respectively. On a log-log scale, the travel angles of land-  
6 320 slides observed in our study linearly decrease with landslide volume, indicating an exponential increase  
7 321 in runout distance with landslide volume. We observed that deep-seated landslides generally exhibited  
8 322 higher volumes and lower travel angles than shallow landslides, but that both landslide types follow the  
9 323 same volume-to-travel angle relationship (c.f. power law fit (a) in Fig. 4).

16 324  
17 325 The coastal erosion of the peninsulas within Tauranga Harbour, ensuing after the post-glacial transgres-  
18 326 sion, was likely to be accompanied by different forms of mass wasting, such as landslides. Therefore,  
19 327 we posited that studying the record of nearshore sediments would enable us to recognize dimensions of  
20 328 landslides that occurred along Omokoroa's coast in the past. The seismic and bathymetry data cover the  
21 329 subtidal nearshore area off northwest Omokoroa and provide a three-dimensional view of four sedimen-  
22 330 tary units (Units 1 to 4) identified within the upper 15 m below the sea surface (Figs. 1A and 5). The  
23 331 basal Unit 1 is characterized by high impedance with little internal structure. The upper boundary of  
24 332 Unit 1 is defined by an undulating reflector having several peaks that are commonly separated by ter-  
25 333 raced troughs. The overlying Unit 2a is internally characterized by numerous reflectors of varying ori-  
26 334 entation. We identified a channel-like structure within this unit (Unit 2b) with cross-bedded reflectors.  
27 335 The overlying Unit 3a truncates the top reflector and some of the internal inclined reflectors of the chan-  
28 336 nel-like Unit 2b. Unit 3b truncates Units 2a, 2b, and 3a. Both truncating units are of low impedance.  
29 337 Unit 3a exhibits some poorly defined chaotic internal reflectors with preferred inclination towards the  
30 338 northwest, whereas Unit 3b is horizontally oriented without any internal reflectors. Units 2 and 3 are  
31 339 overlain by a thin slope-parallel unit (Unit 4), which is recognizable in the shallow southeast area of the  
32 340 near-shore waters.

45 341  
46 342 We interpret the basal Unit 1 to be the local basement consisting of the Waiteariki Ignimbrite. Unit 2  
47 343 represents estuarine and fluvial volcanogenic sediments of mainly volcanogenic origin from the eroded  
48 344 Waiteariki Ignimbrite and newer ignimbrites and multiple tephra-fall deposits, such as the Te Puna Ig-  
49 345 nimbrite and Pahoia Tephra, respectively. The younger Units 3a and 3b are erosive by nature and ex-  
50 346 hibit either chaotic internal reflectors or no reflector at all. We therefore interpret them to be deposits of  
51 347 two major pre-historic landslide events that occurred at Omokoroa at the end of the post-glacial trans-  
52 348 gression when the coastline of Omokoroa was located close to that of the present day.

58 349

350 Given the close proximity to Omokoroa, it is possible that the pre-historic landslide deposits are com-  
351 posed of sensitive halloysitic tephra materials originating from the lower Pahoia Tephra. This interpre-  
352 tation is supported by the findings of Jorat et al. (2017), who identified Pahoia Tephra landslide deposits  
353 in the eastern part of Tauranga Harbour. The slope-parallel layer (Unit 4) only occurs slightly below the  
354 intertidal zone and is therefore likely composed of sediments influenced by tides or storm waves, or  
355 both. We suggest that the second pre-historic landslide deposits (Unit 3b) in the subtidal area off Omo-  
356 koroa followed a similar sliding mechanism to that of the two deep-seated failures with associated flow  
357 slides (L-9 and L-11). The first pre-historic landslide deposits (Unit 3a) was only observed in few seis-  
358 mic profiles and is therefore not further considered in this stud. We interpolated the extent of the second  
359 pre-historic landslide deposits within the seismic profiles and superimposed the associated thickness and  
360 maximum extent on Fig. 1A. The interpolated thickness of the second pre-historic landslide averages  
361 between 0.5 and 1.5 m. Such a thickness is limited to a small area of the assumed landslide area and  
362 therefore provides only a rough estimate of the original landslide thickness. Assuming some major tidal  
363 erosion of the landslide to have taken place after deposition, we consider a constant layer thickness of 1  
364 m to be the lower limit bounding the original landslide. The area enclosed by the line of maximum extent  
365 and the present-day coastline of Omokoroa is c. 185,000 m<sup>2</sup> and, together with an assumed cliff height  
366 of  $H = 35$  m and a maximal runout distance of  $L = 360$  m, results in a landslide volume of 185,000 m<sup>3</sup>  
367 and a travel angle of  $\beta = 5.5^\circ$ .

368  
369 The volume-to-travel angle relationship of the landslides at Omokoroa are similar to those of other land-  
370 slides in halloysitic soils from Japan and Hong Kong (Chigira et al., 2013; Irfan, 1992; Kirk et al., 1997;  
371 Wang et al., 2014) (Fig. 4), highlighting the applicability of our findings to locations beyond New Zea-  
372 land. We further compared dimensions of landslides in halloysitic tephra deposits with those in other  
373 environments worldwide. When considering landslides with similar volume (e.g.,  $V = 10^6$  m<sup>3</sup>),  
374 subaerial landslides commonly exhibit higher travel angles, whereas submarine landslides and quick  
375 clay landslides have smaller travel angles than landslides in halloysitic soil (Edgers and Karlsrud, 1982;  
376 Hampton et al., 1996; Hsu, 1975; L'Heureux et al., 2012; Nicoletti and Sorriso-Valvo, 1991;  
377 Scheidegger, 1973). The comparison with other environments illustrates that landslides in halloysitic  
378 soil exhibit travel angles between those of subaerial and submarine and quick clay landslides. A likely  
379 explanation for this observation is that weathered tephra deposits along the coast of Omokoroa exhibit  
380 high sensitivities, however not being considered as quick clays (Kluger et al., 2017; Torrance, 1983,  
381 1992). Therefore, the travel angles of landslides at Omokoroa are between landslides in quick clays and  
382 (non-sensitive) terrestrial soils.

## 57 384 **5. RAINFALL THRESHOLD FOR HALLOYSITIC TEPHRA DEPOSITS**

### 59 385 **5.1. Rainfall-induced pore water pressure increase**

386 We analyzed the pore water pressure increase due to rainfall in order to better understand the trigger  
1 387 mechanisms of rainfall-induced landsliding in halloysitic tephtras. The low-permeability tephtras (includ-  
2 388 ing the highly sensitive layer) in the lower Pahoia Tephtras act as a water infiltration barrier, creating an  
3 389 overlying unconfined aquifer and an underlying confined aquifer in the slope at Bramley Drive  
4 390 (Fig. 2C). Based on data from the middle piezometer, the water table in the overlying unconfined aquifer  
5 391 is located at an average depth of around 15 m and it exhibits small seasonal but no long-term annual  
6 392 variations (Fig. 3A). The pore water pressure in the unconfined aquifer responds to rainfall events in  
7 393 distinctive spikes, which commonly decay towards background levels within minutes to hours (Fig. 3A  
8 394 and E). We link the distinctive spikes to direct stress transfer from rainwater that infiltrates the capillary  
9 395 fringe of the saturated soil slope above the aquifer. Sometimes the distinctive spikes are followed by  
10 396 smaller pore water pressure increase with longer decay time, which may reflect a temporary rainfall-  
11 397 induced change in gradient of the regional hydraulic head. These smaller pore water pressure increases  
12 398 with longer decay time were not further considered in this study. Based on observations of the lower  
13 399 piezometer, the confined aquifer exhibits small overall variations in pore water pressure, which some-  
14 400 times mimic the seasonal variations and pore water pressure increases with longer decay time observed  
15 401 in the unconfined aquifer (cf. examples 1 and 2 in Fig. 3A). Except for two minor spikes in 2014, we  
16 402 did not observe any pore water pressure increase that resulted from direct rainwater infiltration into the  
17 403 confined aquifer. This lack of direct increase indicates that the confined aquifer exhibits some connec-  
18 404 tion to the regional hydrogeological system, but it is not in direct contact with the unconfined aquifer.  
19  
20  
21  
22  
23  
24  
25  
26  
27  
28  
29  
30  
31  
32

33 406 We enumerated 816 rainfall events within the evaluation period of 4.5 years. Of these, we identified 41  
34 407 large rainfall events, which caused a direct pore water pressure increase in the unconfined aquifer at  
35 408 Bramley Drive (Fig. 3A-B). Some rainfall data of the large rainfall events are taken from the nearest  
36 409 rain gauge at Goodall Road, Whakamarama (cf. light green circles in Fig. 5B).  
37  
38  
39  
40  
41

42 411 We observed some of the largest rainfall events with strong pore water pressure increase during the 2017  
43 412 cyclone season from March to April 2017 (Fig. 3E). The rainfall events cluster in four groups at intervals  
44 413 of one to two weeks and accumulated a total rainfall of more than 800 mm. The pore water pressure  
45 414 increase recorded during the third and fourth group of rainfall events, namely cyclones Debbie and  
46 415 Cook, rank among the highest recorded during the investigation period, and ultimately triggered all 27  
47 416 landslides that occurred at Omokoroa since 2014. We therefore conclude that rainfall and pore water  
48 417 pressure measured at the Bramley Drive landslide are characteristic for the other locations of landslides  
49 418 that occurred across the entire northwest coast of Omokoroa.  
50  
51  
52  
53  
54

## 55 419 56 420 **5.2. Rainfall thresholds**

57 421 We analyzed the rainfall events in order to better understand the role of rainfall intensity and duration  
58 422 in the triggering of landslides and the initiation of effective stress decrease. For this purpose, we plotted  
59  
60  
61  
62  
63  
64  
65

423 the water tables associated with small rainfall events with respect to the rainfall intensity and duration  
424 (grey circles in Fig. 6). We overlaid the small rainfall events with vertical arrows indicating an increase  
425 in water table from the background level due to a large rainfall event. In addition to the change in water  
426 table due to rainfall, we considered the decrease in effective stress in the lower Pahoia Tephra as an  
427 indicator for strength loss in the soil slope (as defined by Eq. 6). Small rainfall events did not induce  
428 any pore water pressure in the unconfined aquifer. The pore water pressure measured at the middle  
429 piezometer during the small rainfall events therefore forms a satisfactory statistical basis for calculating  
430 the background effective stress level within the lower Pahoia Tephra. From long-spaced gamma density  
431 logging in the slope of the Bramley Drive landslide (Kluger et al., 2018), and our long-term piezometer  
432 record during small rainfall events, we calculated a total overburden stress of  $\sigma = 337 \text{ kPa}$  and a pore  
433 water pressure of  $u = 65 \pm 5 \text{ kPa}$ , which yielded a background effective stress of  $\sigma'_b = 272 \pm 5 \text{ kPa}$  at  
434 the middle piezometer (Eq. 6) (cf. Fig. 6B).

435  
436 Large rainfall events temporarily reduce the effective stress in the lower Pahoia Tephra to a different  
437 extent depending on rainfall intensity and duration. The effective stress began to decrease when rainfall  
438 intensities exceeded  $2 \text{ mm/h}$  or at durations of more than  $2.5 \text{ h}$ . The largest effective stress decreases  
439 occurred only when rainfall intensities exceeded  $4 \text{ mm/h}$  or at durations of more than  $4 \text{ h}$ . The large  
440 rainfall events during cyclones Debbie and Cook, preceding the landsliding at Omokoroa, caused the  
441 highest and third-highest effective stress decrease within the studied time period. The rainfall exhibited  
442 remarkably long durations of c.  $25 \text{ h}$  at moderate intensities of  $4 \text{ mm/h}$ . The large June 2018 rainfall  
443 event (as highlighted in Fig. 6B), causing the second-highest effective stress decrease, was not associ-  
444 ated with any landslide event. In comparison to the rainfall events during cyclones Debbie and Cook,  
445 the June 2018 rainfall event exhibits higher rainfall intensity, but a shorter duration of c.  $16 \text{ h}$ . These  
446 observations indicate that in our study area a duration of rainfall above  $16 \text{ h}$  represents a critical level  
447 for landslide triggering. For moderate rainfall intensities ( $I = 4 \text{ mm/h}$ ), we can further constrain this  
448 critical level of rainfall duration to  $25 \text{ h}$ . This finding is in accordance with that of Wei et al. (2018), who  
449 related shallow landslides in Taiwan to rainfall events having durations of more than  $24 \text{ h}$ .

450  
451 Rainfall thresholds are widely used to forecast the likely occurrence of landslides (Guzzetti et al., 2007,  
452 2008; Segoni et al., 2018a). We compared our two rainfall events that triggered landslides since January  
453 2014 with the global rainfall intensity-duration threshold developed by Sidle and Ochiai (2006) (Eq. 7)  
454 and with a regional rainfall duration threshold of Wei et al. (2018). For this purpose, we displayed the  
455 rainfall intensities and durations of all rainfall events that triggered, or did not trigger, landslides together  
456 with the two rainfall thresholds by means of logarithmic and linear scales (Fig. 7). The two rainfall  
457 events that triggered landslides are well constrained by both rainfall thresholds.

459 The influence of rainfall intensity and duration on effective stress decrease was further evaluated by  
 1 460 introducing a normalized effective stress decrease  $\Delta\sigma'_N$ , which quantifies the decrease in effective stress  
 2  
 3 461 from that of the background effective stress in response to large rainfall events (Eq. 8).  
 4  
 5 462

$$7 \text{ 463 } \Delta\sigma'_N = \left(1 - \frac{\sigma'_b - u}{\sigma'_b}\right) \cdot 100 \% \quad (8)$$

9 464  
 10  
 11 465 We consider the normalization of effective stress decrease is less dependent on characteristic features  
 12 466 of our study area, such as depth of the slip surface and aquifer, and hence may be more comparable with  
 13  
 14 467 the results of studies on other soil slopes worldwide. We color-coded the rainfall events into six different  
 15  
 16 468 classes of normalized effective stress decrease (cf. legend in Fig. 7B) and performed the Frequentist  
 17 469 method to calibrate a power law function for the beginning of effective stress decrease, hereafter referred  
 18  
 19 470 to as effective stress threshold (Eq. 9).  
 20

$$21 \text{ 471 } I = 5.19D^{-0.30} \quad (9)$$

22 472  
 23 473  
 24  
 25 474 The effective stress threshold and the rainfall threshold of Sidle and Ochiai (2006) separate the rainfall  
 26 475 events into three regions (indicated by numbers 1 to 3 in Fig. 7A). For each region, we quantified classes  
 27 476 of effective stress decrease by means of frequency distribution (Inset in Fig. 7A). The first region rep-  
 28  
 29 477 represents all rainfall events below the effective stress threshold and mostly consists of small rainfall events  
 30  
 31 478 (99.9%). The second region encompasses all rainfall events between the effective stress threshold and  
 32  
 33 479 the rainfall threshold of Sidle and Ochiai (2006). Around 45 % of the rainfall events showed reductions  
 34  
 35 480 in effective stress mainly in the lower classes 2 and 3, which correspond to normalized effective stress  
 36  
 37 481 decreases between 0 and 15 %. In the third region, above the threshold of Sidle and Ochiai (2006), most  
 38  
 39 482 rainfall events (78 %) caused decreases in effective stress. More than one quarter of rainfall events lie in  
 40  
 41 483 class 6, accounting for normalized effective stress decreases between 28 and 36 %. These rainfall events  
 42  
 43 484 also include the two large rainfall events (cyclones Debbie and Cook in 2017) that triggered landslides  
 44 485 in our study area. The other rainfall events of class 6 exhibit lower rainfall duration, which may be the  
 45  
 46 486 reason why landslides were not triggered during them (Wei et al., 2018). However, a considerable pro-  
 47  
 48 487 portion of rainfall events above the effective stress threshold (regions 2 and 3) did not cause any effec-  
 49 488 tive stress decrease. This finding shows that the effective stress threshold is either not always applicable  
 50  
 51 489 to rainfall events recorded since January 2014 or that other factors, such as antecedent precipitation, soil  
 52  
 53 490 moisture, or locally varying rainfall, may have additionally affected the increase in pore pressure in the  
 54 491 aquifer at Omokoroa (Rahardjo et al., 2005; Segoni et al., 2018a; Segoni et al., 2018b; Yamao et al.,  
 55  
 56 492 2016).  
 57  
 58 493

## 59 494 6. RAINFALL THRESHOLD PREDICTABILITY

495 We validated the capability of the global rainfall threshold by Sidle and Ochiai (2006), and our new  
1 496 effective stress threshold to predict landslides and the initiation of effective stress, respectively. The two  
2  
3 497 contingency matrices, presented in Table 3, classify rainfall events as either true positives (*TP*), true  
4  
5 498 negatives (*TN*), false positives (*FP*), or false negatives (*FN*). The contingency matrices were used to  
6  
7 499 calculate different skill scores of predictive capabilities (sensitivity, specificity, positive prediction  
8  
9 500 power, negative prediction power).

10 501  
11 502 Both thresholds exhibit sensitivities (*Se*) and specificities (*Sp*) close to 1 indicating an overall good  
12  
13 503 predictive capability (Rosi et al., 2015). The positive prediction power (*PPP*) of the rainfall threshold  
14  
15 504 of is 0.056, being at the lower end of values reported in the literature. Rosi et al. (2015) summarized the  
16  
17 505 positive prediction power of numerous rainfall thresholds calibrated for landslides occurrences in the  
18  
19 506 Tuscany region, Italy, and reported values of  $PPP = 0.105 \pm 0.073$ . The lowness in positive prediction  
20  
21 507 power observed in our study is likely because of the small number of rainfall events that triggered land-  
22  
23 508 slides in our study. Another factor is probably because the rainfall threshold of Sidle and Ochiai (2006)  
24  
25 509 does not consider a cutoff value in rainfall duration of, e.g.  $D = 24$  h, which was used by Wei et al.  
26  
27 510 (2018) and which seems to be an important threshold in our study area (cf. Fig. 7). Finally, the positive  
28  
29 511 prediction power of the rainfall threshold of Sidle and Ochiai (2006) may be further influenced by the  
30  
31 512 extraction of rainfall parameters from the rainfall data and the separation of individual rainfall events,  
32  
33 513 which we based on a dry period of six hours (Tiranti and Rabuffetti, 2010). The positive prediction  
34  
35 514 power of the effective stress threshold is 0.526, being a satisfactory value compared to the values re-  
36  
37 515 ported for other rainfall thresholds (Rosi et al., 2015). Hence, the probability of correctly predicting a  
38  
39 516 decrease in effective stress is 53%. The negative prediction power (*NPP*) of both thresholds is close to  
40  
41 517 1, indicating that they are well capable of correctly predicting rainfall events that did not trigger land-  
42  
43 518 slides or that did not cause any decrease in effective stress. The high *NPP* may also be influenced by  
44  
45 519 the relatively small number of rainfall events applied in this study.

46 520  
47 521 For future research we suggest that the investigative time period could be increased as well as the num-  
48  
49 522 ber and spatial distribution of piezometers within the study area. These measures would, on the one  
50  
51 523 hand, provide a larger data base for threshold calibration and validation, and on the other, would prevent  
52  
53 524 local variabilities in the aquifer and moisture conditions of the soil slope from influencing the calibration  
54  
55 525 of the effective stress threshold. Furthermore, it has yet to be tested whether or not the effective stress  
56  
57 526 threshold is also applicable to other soil materials (e.g., sedimentary clays and sands) and environmental  
58  
59 527 constraints (e.g., dry and tropical) that are significantly different from those of our study area. As Segoni  
60  
61 528 et al. (2018a) pointed out in their recent review, implementation of pore water pressure into calibration  
62  
63 529 of the rainfall thresholds would add a beneficial perspective in future landslide prediction studies. We  
64  
65 530 believe that our effective stress threshold contributes towards the implementation of pore water pressure  
66  
67 531 (and decrease in effective stress) into rainfall thresholds for the occurrence of landslides.

532

## 7. CONCLUSIONS

We have studied a ~40-m-thick succession of weathered rhyolitic pyroclastic deposits dating to c. 0.9 Ma that are dominated by halloysite at Omokoroa Peninsula, Tauranga Harbour, the site of multiple landslide events. We showed that for moderate rainfall intensities ( $I = 4$  mm/h) a rainfall duration of 25 h was a critical threshold for landsliding, and that the ensuing landslide dimensions, are both in keeping with parameters reported for landslides in halloysitic tephra deposits in Hong Kong and Japan. The normalized effective stress principle and effective stress threshold developed in our study thus provide a better understanding of the rainfall trigger mechanism of landslides in halloysitic soil materials worldwide. Because the rainfall intensity-duration threshold of Sidle and Ochiai (2006) was reproduced very well by our analyses, not only for the shallow-translational but also for the deep-rotational landslides in our study area, we conclude that the rainfall threshold may be extended to these types of landslides in the future. We also found that:

545

- In our study, landslides were only triggered when rainfall events exceeded both the rainfall threshold of Sidle and Ochiai (2006) as well as the rainfall duration threshold of  $D = 24$  h proposed by Wei et al. (2018).
- A new effective stress threshold was calibrated based on rainfall events that initiated a decrease in effective stress in the slope. The level of effective stress decrease increases with rainfall intensity and duration. We observed highest effective stress decrease of up to 36 % during rainfall events that triggered landslides in our study area.
- The effective stress threshold exhibits a satisfactory predictive capability. The probability of correctly predicting a decrease in effective stress is 53 %. False positives and false negatives are low indicating a high capability of the effective stress threshold to correctly predict rainfall events that did not cause any decrease in effective stress.

557

## ACKNOWLEDGMENTS

This research was funded by the DFG Research Center MARUM of the University of Bremen, Germany, through INTERCOAST and the University of Waikato in Hamilton, New Zealand. We acknowledge the New Zealand Geotechnical Society (NZGS) for funding parts of this project. We thank the Bay of Plenty Regional Council who provided us with the rainfall data from Goodall Road, Whakamarama. We thank Dirk Immenga, Jimmy Van der Pauw, and Wade Roest for conducting the bathymetric and seismic surveys, and Ben Campbell who helped with the field descriptions of the landslides. We gratefully acknowledge Matt Ikari who provided helpful comments on the manuscript. The article is an output of the EXTRAS project “EXTending TephRAS as a global geoscientific research tool stratigraphically, spatially, analytically, and temporally” led by the International Focus Group on Tephrochronology and

568 Volcanism (INTAV) of the Stratigraphy and Chronology Commission (SACCOM) of the International  
1 569 Union for Quaternary Research (INQUA) for 2015–2019.  
2

3 570

4  
5 571 **REFERENCE CITED**

- 6  
7 572 - Adamo, P., Violante, P., and Wilson, M., 2001, Tubular and spheroidal halloysite in pyroclastic  
8 573 deposits in the area of the Roccamonfina volcano (Southern Italy): *Geoderma*, v. 99, no. 3, p.  
9 574 295-316.
- 10 575 - Agostini, A., Tofani, V., Nolesini, T., Gigli, G., Tanteri, L., Rosi, A., Cardellini, S., and Casagli,  
11 576 N., 2014, A new appraisal of the Ancona landslide based on geotechnical investigations and  
12 577 stability modelling: *Quarterly journal of engineering geology and hydrogeology*, v. 47, no. 1,  
13 578 p. 29-43.
- 14 579 - Askenasy, P., Dixon, J., and McKee, T., 1973, Spheroidal halloysite in a Guatemalan soil: *Soil  
15 580 Science Society of America Journal*, v. 37, no. 5, p. 799-803.
- 16 581 - Assier-Rzadkiewicz, S., Heinrich, P., Sabatier, P., Savoye, B., and Bourillet, J., 2000, Numerical  
17 582 modelling of a landslide-generated tsunami: the 1979 Nice event: *Pure and Applied  
18 583 Geophysics*, v. 157, no. 10, p. 1707-1727.
- 19 584 - Basher, L. R., 2013, Erosion processes and their control in New Zealand: *Ecosystem services in  
20 585 New Zealand—conditions and trends*, v. 2013, p. 363-374.
- 21 586 - Baum, R. L., and Godt, J. W., 2010, Early warning of rainfall-induced shallow landslides and  
22 587 debris flows in the USA: *Landslides*, v. 7, no. 3, p. 259-272.
- 23 588 - Birrell, K., Fieldes, M., and Williamson, K., 1955, Unusual forms of halloysite: *American  
24 589 Mineralogist*, v. 40, no. 1-2, p. 122-124.
- 25 590 - Briggs, R., Hall, G., Harmsworth, G., Hollins, A., Houghton, B., Hughes, G., Morgan, M., and  
26 591 Whitbread-Edwards, A., 1996, *Geology of the Tauranga area*: Department of Earth Sciences,  
27 592 University of Waikato.
- 28 593 - Briggs, R., Houghton, B., McWilliams, M., and Wilson, C., 2005, <sup>40</sup>Ar/<sup>39</sup>Ar ages of silicic  
29 594 volcanic rocks in the Tauranga- Kaimai area, New Zealand: dating the transition between  
30 595 volcanism in the Coromandel Arc and the Taupo Volcanic Zone: *New Zealand Journal of  
31 596 Geology and Geophysics*, v. 48, no. 3, p. 459-469.
- 32 597 - Brunetti, M., Peruccacci, S., Rossi, M., Luciani, S., Valigi, D., and Guzzetti, F., 2010, Rainfall  
33 598 thresholds for the possible occurrence of landslides in Italy: *Natural Hazards and Earth  
34 599 System Sciences*, v. 10, no. 3, p. 447-458.
- 35 600 - Caine, N., 1980, The rainfall intensity-duration control of shallow landslides and debris flows:  
36 601 *Geografiska annaler: series A, physical geography*, v. 62, no. 1-2, p. 23-27.
- 37 602 - Chappell, J., 1975, Upper Quaternary warping and uplift rates in the Bay of Plenty and west coast,  
38 603 North Island, New Zealand: *New Zealand journal of geology and geophysics*, v. 18, no. 1, p.  
39 604 129-154.
- 40 605 - Chigira, M., 2014, Geological and geomorphological features of deep-seated catastrophic  
41 606 landslides in tectonically active regions of Asia and implications for hazard mapping:  
42 607 *Episodes*, v. 37, no. 4, p. 284-294.
- 43 608 - Chigira, M., Nakasuji, A., Fujiwara, S., and Sakagami, M., 2013, Catastrophic landslides of  
44 609 pyroclastics induced by the 2011 off the Pacific coast of Tohoku Earthquake, *Earthquake-  
45 610 Induced Landslides*, Springer, p. 139-147.
- 46 611 - Chigira, M., and Yokoyama, O., 2005, Weathering profile of non-welded ignimbrite and the water  
47 612 infiltration behavior within it in relation to the generation of shallow landslides: *Engineering  
48 613 geology*, v. 78, no. 3, p. 187-207.
- 49 614 - Churchman, G. J., and Lowe, D. J., 2012, Alteration, formation, and occurrence of minerals in  
50 615 soils, in Huang, P. M., Li, Y., and Sumner, M. E., eds., *Handbook of Soil Sciences. Properties  
51 616 and Processes*, 2nd edition USA, CRC Press, p. 20.21-20.72.
- 52 617 - Cravero, F., and Churchman, G. J., 2016, The origin of spheroidal halloysites: a review of the  
53 618 literature: *Clay Minerals*, v. 51, no. 3, p. 417-427.
- 54 619 - Crozier, M., 2005, Multiple-occurrence regional landslide events in New Zealand: hazard  
55 620 management issues: *Landslides*, v. 2, no. 4, p. 247-256.
- 56  
57  
58  
59  
60  
61  
62  
63  
64  
65

- 621 - Cruden, D. M., and Varnes, D. J., 1996, Landslides: investigation and mitigation. Chapter 3-  
1 622       Landslide types and processes: Transportation research board special report, no. 247.
- 2 623 - Cunningham, M. J., Lowe, D. J., Wyatt, J. B., Moon, V. G., and Jock Churchman, G., 2016,  
3 624       Discovery of halloysite books in altered silicic Quaternary tephtras, northern New Zealand:  
4 625       Clay Minerals, v. 51, no. 3, p. 351-372.
- 5 626 - de Lange, W., 1993, Wave Climate for No. 1 Reach, Port of Tauranga, Tauranga Harbour, Report  
6 627       to the Port of Tauranga Ltd: Hamilton, New Zealand.: Department of Earth Sciences,  
7 628       University of Waikato.
- 8 629 - De Oliveira, M. T., Furtado, S., Formoso, M. L., Eggleton, R. A., and Dani, N., 2007, Coexistence  
9 630       of halloysite and kaolinite: a study on the genesis of kaolin clays of Campo Alegre Basin,  
10 631       Santa Catarina State, Brazil: Anais da Academia Brasileira de Ciências, v. 79, no. 4, p. 665-  
11 632       681.
- 12 633 - Demers, D., Robitaille, D., Locat, P., and Potvin, J., 2014, Inventory of large landslides in  
13 634       sensitive clay in the province of Québec, Canada: preliminary analysis, *in* L'Heureux, J.-S.,  
14 635       Locat, A., Leroueil, S., Demers, D., and Locat, J., eds., Landslides in Sensitive Clays: From  
15 636       Geosciences to Risk Management: Dordrecht, Springer Netherlands, p. 77-89.
- 16 637 - Duncan, J. M., Wright, S. G., and Brandon, T. L., 2014, Soil strength and slope stability, John  
17 638       Wiley & Sons.
- 18 639 - Edgers, L., and Karlsrud, K., 1982, Soil flows generated by submarine slides: Case studies and  
19 640       consequences: Nor. Geotech. Inst. Bull, v. 143, p. 1-11.
- 20 641 - Gulliver, C., and Houghton, B., 1980, Omokoroa Point Land Stability Investigation: Tonkin &  
21 642       Taylor.
- 22 643 - Guzzetti, F., Ardizzone, F., Cardinali, M., Rossi, M., and Valigi, D., 2009, Landslide volumes and  
23 644       landslide mobilization rates in Umbria, central Italy: Earth and Planetary Science Letters, v.  
24 645       279, no. 3-4, p. 222-229.
- 25 646 - Guzzetti, F., Peruccacci, S., Rossi, M., and Stark, C. P., 2007, Rainfall thresholds for the initiation  
26 647       of landslides in central and southern Europe: Meteorology and atmospheric physics, v. 98, no.  
27 648       3-4, p. 239-267.
- 28 649 - -, 2008, The rainfall intensity–duration control of shallow landslides and debris flows: an update:  
29 650       Landslides, v. 5, no. 1, p. 3-17.
- 30 651 - Hampton, M. A., Lee, H. J., and Locat, J., 1996, Submarine landslides: Reviews of geophysics, v.  
31 652       34, no. 1, p. 33-59.
- 32 653 - Houghton, B., and Cuthbertson, A., 1989, Sheet T14BD Kaimai; Geological Map of New Zealand  
33 654       1: 50,000: Dept. Sci. Indus. Res., Wellington, New Zealand.
- 34 655 - Hsu, K. J., 1975, Catastrophic debris streams (sturzstroms) generated by rockfalls: Geological  
35 656       Society of America Bulletin, v. 86, no. 1, p. 129-140.
- 36 657 - Imbert, T., and Desprairies, A., 1987, Neoformation of halloysite on volcanic glass in a marine  
37 658       environment: Clay Minerals, v. 22, no. 2, p. 179-185.
- 38 659 - Irfan, T., 1992, Mineralogical assessment of creep-type instability at two landslip sites:  
39 660       Geotechnical Engineering office.
- 40 661 - -, 1998, Structurally controlled landslides in saprolitic soils in Hong Kong: Geotechnical &  
41 662       Geological Engineering, v. 16, no. 3, p. 215-238.
- 42 663 - Jeong, G., and Kim, S., 1996, Morphology of halloysite particles and aggregates in the weathering  
43 664       of anorthosite: Journal of the Mineralogical Society of Korea, v. 9, p. 64-70.
- 44 665 - Jorat, M. E., Moon, V. G., Hepp, D. A., Kreiter, S., de Lange, W. P., Feldmann, S., and Mörz, T.,  
45 666       2017, Subseafloor investigation of sediments at Southern Tauranga Harbour, New Zealand,  
46 667       before capital dredging: Journal of Coastal Research, v. 33, no. 2, p. 227-242.
- 47 668 - Joussein, E., Petit, S., Churchman, J., Theng, B., Righi, D., and Delvaux, B., 2005, Halloysite clay  
48 669       minerals—a review: Clay Minerals, v. 40, no. 4, p. 383-426.
- 49 670 - Kirk, P., Campbell, S., Fletcher, C., and Merriman, R., 1997, The significance of primary volcanic  
50 671       fabrics and clay distribution in landslides in Hong Kong: Journal of the Geological Society, v.  
51 672       154, no. 6, p. 1009-1019.
- 52 673 - Kirkman, J., 1977, Possible structure of halloysite disks and cylinders observed in some New  
53 674       Zealand rhyolitic tephtras: Clay Minerals, v. 12, p. 199.
- 54 675 - Kluger, M. O., Kreiter, S., Moon, V., Orense, R. P., Mills, P., and Moertz, T., 2018, Undrained  
55 676       cyclic shear behaviour of weathered tephra Géotechnique.

- 677 - Kluger, M. O., Moon, V. G., Kreiter, S., Lowe, D. J., Churchman, G., Hepp, D. A., Seibel, D.,  
1 678 Jorat, M. E., and Mörz, T., 2017, A new attraction-detachment model for explaining flow  
2 679 sliding in clay-rich tephra: *Geology*, v. 42, no. 2, p. 131-134.
- 3 680 - Kvalstad, T. J., Andresen, L., Forsberg, C. F., Berg, K., Bryn, P., and Wangen, M., 2005, The  
4 681 Storegga slide: evaluation of triggering sources and slide mechanics: *Marine and Petroleum*  
5 682 *Geology*, v. 22, no. 1, p. 245-256.
- 6 683 - L'Heureux, J.-S., Eilertsen, R. S., Glimsdal, S., Issler, D., Solberg, I.-L., and Harbitz, C. B., 2012,  
7 684 The 1978 quick clay landslide at Rissa, mid Norway: subaqueous morphology and tsunami  
8 685 simulations, *Submarine mass movements and their consequences*, Springer, p. 507-516.
- 9 686 - L'Heureux, J.-S., Locat, A., Leroueil, S., Demers, D., and Locat, J., 2014, Landslides in Sensitive  
10 687 Clays—From Geosciences to Risk Management, *Landslides in Sensitive Clays*, Springer, p. 1-  
11 688 12.
- 12 689 - Labuz, J. F., and Zang, A., 2012, Mohr–Coulomb failure criterion: *Rock mechanics and rock*  
13 690 *engineering*, v. 45, no. 6, p. 975-979.
- 14 691 - Larsen, I. J., Montgomery, D. R., and Korup, O., 2010, Landslide erosion controlled by hillslope  
15 692 material: *Nature Geoscience*, v. 3, no. 4, p. 247.
- 16 693 - Longva, O., Janbu, N., Blikra, L., and Bøe, R., 2003, The 1996 Finneidfjord slide; seafloor failure  
17 694 and slide dynamics, *Submarine Mass movements and their consequences*, Springer, p. 531-  
18 695 538.
- 19 696 - Loughnan, F., and Roberts, F. I., 1981, The natural conversion of ordered kaolinite to halloysite (1  
20 697 at Burning Mountain near Wingen'New South Wales: *American Mineralogist*, v. 66, p. 997-  
21 698 1005.
- 22 699 - Lowe, D. J., 2011, Tephrochronology and its application: a review: *Quaternary Geochronology*, v.  
23 700 6, no. 2, p. 107-153.
- 24 701 - Malamud, B. D., Turcotte, D. L., Guzzetti, F., and Reichenbach, P., 2004, Landslides,  
25 702 earthquakes, and erosion: *Earth and Planetary Science Letters*, v. 229, no. 1-2, p. 45-59.
- 26 703 - Martelloni, G., Segoni, S., Fanti, R., and Catani, F., 2012, Rainfall thresholds for the forecasting  
27 704 of landslide occurrence at regional scale: *Landslides*, v. 9, no. 4, p. 485-495.
- 28 705 - Moon, V., de Lange, W., Garae, C., Mörz, T., Jorat, M., and Kreiter, S., 2015a, Monitoring the  
29 706 landslide at Bramley Drive, Tauranga, NZ.
- 30 707 - Moon, V. G., Lowe, D. J., Cunningham, M. J., Wyatt, J. B., de Lange, W. P., Churchman, G. J.,  
31 708 Mörz, T., Kreiter, S., Kluger, M. O., and Jorat, M. E., Sensitive pyroclastic-derived halloysitic  
32 709 soils in northern New Zealand: Interplay of microstructure, minerals, and geomechanics, *in*  
33 710 *Proceedings Volcanic Rocks and Soils 2015b*, Taylor and Francis, London, p. 3-21.
- 34 711 - Napolitano, E., Fusco, F., Baum, R. L., Godt, J. W., and De Vita, P., 2016, Effect of antecedent-  
35 712 hydrological conditions on rainfall triggering of debris flows in ash-fall pyroclastic mantled  
36 713 slopes of Campania (southern Italy): *Landslides*, v. 13, no. 5, p. 967-983.
- 37 714 - Nicoletti, P. G., and Sorriso-Valvo, M., 1991, Geomorphic controls of the shape and mobility of  
38 715 rock avalanches: *Geological Society of America Bulletin*, v. 103, no. 10, p. 1365-1373.
- 39 716 - Norsk Geoteknisk Forening, 1974, Retningslinjer for presentasjon av geotekniske undersøkelser:  
40 717 Oslo, Norway, v. 16.
- 41 718 - Parham, W. E., 1970, SP-10 Clay Mineralogy and Geology of Minnesota's Kaolin Clays.
- 42 719 - Parry, S., Campbell, S., and Churchman, G., Kaolin-Rich Zones In Hong Kong Saprolites Their  
43 720 Interpretation And Engineering Significance, *in Proceedings ISRM International*  
44 721 *Symposium 2000*, International Society for Rock Mechanics.
- 45 722 - -, 2001, The origin and shear strength of kaolin-rich zones in Hong Kong: *Geotech. Engn*, p. 893-  
46 723 897.
- 47 724 - Peruccacci, S., Brunetti, M. T., Luciani, S., Vennari, C., and Guzzetti, F., 2012, Lithological and  
48 725 seasonal control on rainfall thresholds for the possible initiation of landslides in central Italy:  
49 726 *Geomorphology*, v. 139, p. 79-90.
- 50 727 - Pouclet, A., Cambay, H., Cadet, J.-P., Bourgois, J., and De Wever, P., 28. VOLCANIC ASH  
51 728 FROM LEG 112 OFF PERU1, *in Proceedings Proceedings of the Ocean Drilling Program:*  
52 729 *Scientific results 1990*, The Program, p. 465.
- 53 730 - Quantin, P., and Rambaud, D., 1987, Genesis of spherical halloysite from basaltic ash, at Ambrym  
54 731 (Vanuatu).

- 732 - Quayle, A., 1984, The climate and weather of the Bay of Plenty region, Ministry of Transport,  
 1 733 New Zealand Meteorological Service.
- 2 734 - Rahardjo, H., Lee, T., Leong, E. C., and Rezaur, R., 2005, Response of a residual soil slope to  
 3 735 rainfall: Canadian Geotechnical Journal, v. 42, no. 2, p. 340-351.
- 4 736 - Romero, R., Robert, M., Elsass, F., and Garcia, C., 1992, Abundance of halloysite neof ormation in  
 5 737 soils developed from crystalline rocks. Contribution of transmission electron microscopy:  
 6 738 Clay Minerals, v. 27, no. 1, p. 35-46.
- 7 739 - Rosi, A., Lagomarsino, D., Rossi, G., Segoni, S., Battistini, A., and Casagli, N., 2015, Updating  
 8 740 EWS rainfall thresholds for the triggering of landslides: Natural Hazards, v. 78, no. 1, p. 297-  
 9 741 308.
- 10 742 - Rösner, A., 2016, Impact of seismicity on Nice's slope stability [M.Sc.: University of Bremen.
- 11 743 - Saigusa, M., Shoji, S., and Kato, T., 1978, Origin and nature of halloysite in Ando soils from  
 12 744 Towada tephra, Japan: Geoderma, v. 20, no. 2, p. 115-129.
- 13 745 - Scheidegger, A. E., 1973, On the prediction of the reach and velocity of catastrophic landslides:  
 14 746 Rock Mechanics and Rock Engineering, v. 5, no. 4, p. 231-236.
- 15 747 - Segoni, S., Piciullo, L., and Gariano, S. L., 2018a, A review of the recent literature on rainfall  
 16 748 thresholds for landslide occurrence: Landslides, v. 15, no. 8, p. 1483-1501.
- 17 749 - Segoni, S., Rosi, A., Lagomarsino, D., Fanti, R., and Casagli, N., 2018b, Brief communication:  
 18 750 Using averaged soil moisture estimates to improve the performances of a regional-scale  
 19 751 landslide early warning system: Natural Hazards and Earth System Sciences, v. 18, no. 3, p.  
 20 752 807-812.
- 21 753 - Shaller, P., Sykora, D., Doroudian, M., and Churchman, G. J., 2016, Rapid in situ conversion of  
 22 754 late-stage volcanic materials to halloysite implicated in catastrophic dam failure, Hawaii: Clay  
 23 755 Minerals, v. 51, no. 3, p. 499-515.
- 24 756 - Shepherd, M., Betts, H., McFadgen, B., and Sutton, D., 2000, Geomorphological evidence for a  
 25 757 Pleistocene barrier at Matakana Island, Bay of Plenty, New Zealand: New Zealand Journal of  
 26 758 Geology and Geophysics, v. 43, no. 4, p. 579-586.
- 27 759 - Sidle, R. C., and Ochiai, H., 2006, Landslides: processes, prediction, and land use, Washington,  
 28 760 DC, American Geophysical Union, Water resources monograph series.
- 29 761 - Sieffermann, G., and Millot, G., Equatorial and tropical weathering of recent basalts from  
 30 762 Cameroon: allophanes, halloysite, metahalloysite, kaolinite and gibbsite, *in* Proceedings  
 31 763 Proceedings of the International Clay Conference, Tokyo1969, Volume 1, Israel University  
 32 764 Press, Jerusalem, p. 417-430.
- 33 765 - Singer, A., Zarei, M., Lange, F., and Stahr, K., 2004, Halloysite characteristics and formation in  
 34 766 the northern Golan Heights: Geoderma, v. 123, no. 3, p. 279-295.
- 35 767 - Skempton, A., and Northey, R., 1952, The sensitivity of clays: Geotechnique, v. 3, no. 1, p. 30-53.
- 36 768 - Smalley, I., Ross, C. W., and Whitton, J., 1980, Clays from New Zealand support the inactive  
 37 769 particle theory of soil sensitivity: Nature, v. 288, p. 576-577.
- 38 770 - Tanaka, K., 1992, Slope hazards and clay minerals: Nendo Kagaku, v. 32, no. 1, p. 16-22.
- 39 771 - Taskey, R. D., 1977, Relationships of clay mineralogy to landscape stability in Western Oregon.
- 40 772 - Tiranti, D., and Rabuffetti, D., 2010, Estimation of rainfall thresholds triggering shallow  
 41 773 landslides for an operational warning system implementation: Landslides, v. 7, no. 4, p. 471-  
 42 774 481.
- 43 775 - Torrance, J. K., 1983, Towards a general model of quick clay development: Sedimentology, v. 30,  
 44 776 no. 4, p. 547-555.
- 45 777 - -, 1992, Discussion on sensitivity to remoulding of some volcanic ash soils in New Zealand, by D.  
 46 778 Jacquet: Engineering Geology, v. 32, no. 1, p. 101-105.
- 47 779 - Varnes, D. J., 1978, Slope movement types and processes: Special report, v. 176, p. 11-33.
- 48 780 - Wada, K., and Kakuto, Y., 1985, Embryonic halloysites in Ecuadorian soils derived from volcanic  
 49 781 ash: Soil Science Society of America Journal, v. 49, no. 5, p. 1309-1318.
- 50 782 - Wang, G., Suemine, A., Zhang, F., Hata, Y., Fukuoka, H., and Kamai, T., 2014, Some fluidized  
 51 783 landslides triggered by the 2011 Tohoku Earthquake (M w 9.0), Japan: Geomorphology, v.  
 52 784 208, p. 11-21.
- 53 785 - Wei, L.-W., Huang, C.-M., Chen, H., Lee, C.-T., Chi, C.-C., and Chiu, C.-L., 2018, Adopting the I  
 54 786 3-R 24 rainfall index and landslide susceptibility for the establishment of an early warning

787 model for rainfall-induced shallow landslides: *Natural Hazards & Earth System Sciences*, v.  
1 788 18, no. 6.  
2 789 - Wen, B., and Aydin, A., 2003, Microstructural study of a natural slip zone: quantification and  
3 790 deformation history: *Engineering Geology*, v. 68, no. 3, p. 289-317.  
4 791 - Yamao, M., Sidle, R., Gomi, T., and Imaizumi, F., 2016, Characteristics of landslides in unwelded  
5 792 pyroclastic flow deposits, southern Kyushu, Japan: *Natural Hazards and Earth System*  
6 793 *Sciences*, v. 16, no. 2, p. 617-627.  
7 794 - Zaruba, Q., and Mencl, V., 2014, *Landslides and their control*, Elsevier.  
8 795  
9

10  
11  
12  
13  
14  
15  
16  
17  
18  
19  
20  
21  
22  
23  
24  
25  
26  
27  
28  
29  
30  
31  
32  
33  
34  
35  
36  
37  
38  
39  
40  
41  
42  
43  
44  
45  
46  
47  
48  
49  
50  
51  
52  
53  
54  
55  
56  
57  
58  
59  
60  
61  
62  
63  
64  
65

796 **FIGURE CAPTIONS**

1  
2 797 **Fig. 1. Study area. A:** Distribution of coastal landslides along the northwest coast of Omokoroa. The  
3 798 topographic map is overlain by landslide main scarps, landslide dimensions, and bathymetry data from  
4  
5 799 the near shore area. **B:** Location of Omokoroa Peninsula within the estuarine lagoon of Tauranga Har-  
6  
7 800 bour, northern New Zealand. **C-E:** Photographs of coastal landslides at Omokoroa. The locations are  
8 801 indicated in Fig. 1A. Maps in Fig. 1 were created by using a 250-m-resolution national bathymetry  
9 802 grid, provided by NIWA, licensed under NODL By-NN-NC-Sa 1.0, an 8-m-resolution regional digital  
10 803 elevation model, and a 1-m-resolution local LIDAR digital elevation model, both provided by LINZ,  
11  
12 804 licensed under CC BY 4.0.

13  
14  
15 805  
16  
17 806 **Fig. 2. Geology of the 1979 Bramley Drive landslide. A:** Stratigraphy of the succession of lignite,  
18 807 ignimbrite, and tephra-fall deposits, and intervening paleosols (P). **B:** Relative concentrations of dif-  
19  
20 808 ferent halloysite clay morphologies with depth (after Kluger et al., 2017). **C:** Cross-section of the 1979  
21 809 Bramley Drive landslide showing the locations of the confined and unconfined aquifers, respectively,  
22 810 with locations of upper (U), middle (M), and lower (L) piezometers. Upper and lower tidal ranges are  
23 811 from de Lange (1993). **D:** Scanning electron microscope images of mushroom cap-shaped spheroidal  
24  
25 812 halloysite, which is abundant in the highly sensitive layer within the Pahoia Tephra. The images are  
26 813 modified with permission from Kluger et al. (2017), copyright 2017 The Geological Society of Amer-  
27  
28 814 ica.

29  
30 815  
31  
32 816  
33 817 **Fig. 3 Pore water pressure (PWP) and rainfall characteristics. A-B:** PWP and hourly rainfall time  
34 818 series from January 2014 to June 2018. Green circles indicate large rainfall events (defined in the text)  
35 819 having been taken from rain gauges at the Bramley Drive landslide (dark green) or at Goodall Road,  
36 820 Whakamarama (light green). **C-D:** Rainfall correlations between rain gauges at Bramley Drive land-  
37 821 slide and Goodall Road, Whakamarama. **E:** Hourly rainfall, PWP, and number of recent landslides  
38  
39 822 during the 2017 cyclone season.

40  
41  
42 823 **Fig. 4. Landslide dimensions.**  $r^2$  is the coefficient of determination.

43  
44  
45 824  
46  
47 825 **Fig. 5. Sedimentary architecture of the subtidal area, northwest Omokoroa. A:** Along-shore and  
48 826 **B:** cross-shore seismic profiles and interpretation of seismic units.

49  
50 827  
51  
52 828 **Fig. 6. Effect of rainfall events on effective stress decrease.** Changes in water table and effective  
53 829 stress in the soil slope of the Bramley Drive landslide with **A:** rainfall intensity and **B:** duration of  
54 830 rainfall events. The length of arrows indicates the change in water table and effective stress, respec-  
55 831 tively. The colors of the arrows represent the increase in water table as defined in the color scale.

56  
57 832

58  
59  
60  
61  
62  
63  
64  
65

833 **Fig. 7. Rainfall thresholds** Rainfall intensity-duration relationships of small and large rainfall events  
 834 plotted on **A:** logarithmic and **B:** linear scales. The black dashed lines represent the two rainfall  
 835 thresholds proposed by Sidle and Ochiai (2006) and Wei et al. (2018). The black line represents the  
 836 effective stress threshold, which is calibrated for the lower bound of large rainfall events at the 5 %  
 837 confidence interval. The colors of symbols and of the stacked bar chart are defined in the legend of  
 838 Fig. 7B.

## 840 TABLES

841 **Table 1.** Coastal landslides at Omokoroa Peninsula, Tauranga Harbour, New Zealand.

Land -slide No.	Location	Material composition	Type	Landslide dimension										Timing
				$D_s$	$W_s$	$L_s$	$H$	$L$	$A_L$	$V_T$	$V_r$	$H/L$	$\beta$	
				m	m	m	m	m	m <sup>2</sup>	m <sup>3</sup>	m <sup>3</sup>		°	
L-1	Waterview Ter	TPI, PT*	D <sup>S</sup>	7	25	25	20	30	625		2,291	0.67	34	A
L-2	Hamurana	TPI*, PT	S		185	6	5	8	1,185	1,811		0.67	34	A
L-3-1	Rd –	TPI	S		30	32	20	50	960	1,370		0.40	22	A
L-3-2	Kaharoa Av	TPI*, PT	D	5.5	15	14	10	20	212		611	0.50	27	A
L-3-3		PT	S		5	10	7	10	49	26		0.70	35	A
L-4	Kaharoa Av	N/A	D <sup>S</sup>	4	15	16	10	12	234		491	0.83	40	A
L-5	Kowai Grv	TPI, PT*	D	9	30	32	20	38	960		4,526	0.53	28	A
L-6		TPI	S		29	29	20	21	841	1,148		0.95	44	A
L-7	McDonnell St	N/A	S		20	25	15	25	500	574		0.60	31	A
L-8		TPI	S		48	9	8	5	410	441		1.60	58	A
L-9		TPI, PT*	D <sup>S</sup>	14	25	58	30	115	1,458		10,686	0.26	15	A
L-10	Bramley Dr	PT, HA	S		64	36	30	30	2,308	4,403		1.00	45	A
L-11		PT, HA	D	27	62	68	32	210	4,216		59,602	0.15	9	1979†
L-12		PT, HA	S		10	17	15	15	170	136		1.00	45	A‡, B
L-13	Ruamoana Pl	PT, HA	S		14	25	21	25	343	348		0.85	41	A
L-14		PT	D	6	19	15	9	30	278		872	0.30	17	B
L-15		PT	D	7	15	15	9	30	225		825	0.30	17	B
L-16	Myrtle Dr	TPI*, PT	D	4	14	17	8	25	235		491	0.32	18	A‡, B
L-17		TPI	S		15	9	8	10	142	107		0.80	39	A
L-18		TPI	S		30	18	15	20	541	637		0.75	37	B
L-19	Crapp Historic Reserve	TPI, PT, HA	S		35	14	14	10	484	550		1.35	53	A
L-20		TPI, PT, HA	S		7	20	20	10	142	107		2.00	63	A
L-21		TPI, PT, HA	S		25	12	12	10	309	303		1.20	50	A
L-22		TPI, PT, HA	S		15	11	10	20	168	134		0.50	27	A
L-23		TPI, PT, HA	S		8	13	13	7	107	73		1.86	62	A
L-24		TPI, PT, HA	S		11	14	14	6	152	118		2.25	66	A
L-25		TPI, PT, HA	S		21	12	10	10	257	236		0.95	44	A
L-26	Harbour View Rd	TPI	D <sup>S</sup>	6	20	28	19	50	552		1,733	0.38	21	A

842 \*Base of slide surface

843 †1979 Bramley Drive landslide dimensions from Gulliver and Houghton (1980)

844 ‡Main failure event

845 Ter–Terrace; Rd–Road; Av–Avenue; Grv–Grove; St–Street; Dr–Drive; Pl–Place

846 TPI–Te Puna Ignimbrite; PT–Pahoia Tephra; HA–Hamilton Ashes; N/A–Not available

847 D–deep-seated; S–shallow; D<sup>S</sup>–complex earth slide with deep-seated being the dominant mode of failure and  
 848 shallow failure associated to the main event

849 A–Cyclone Debbie (April 5<sup>th</sup>, 2017); B–Cyclone Cook (April 13<sup>th</sup>, 2017)

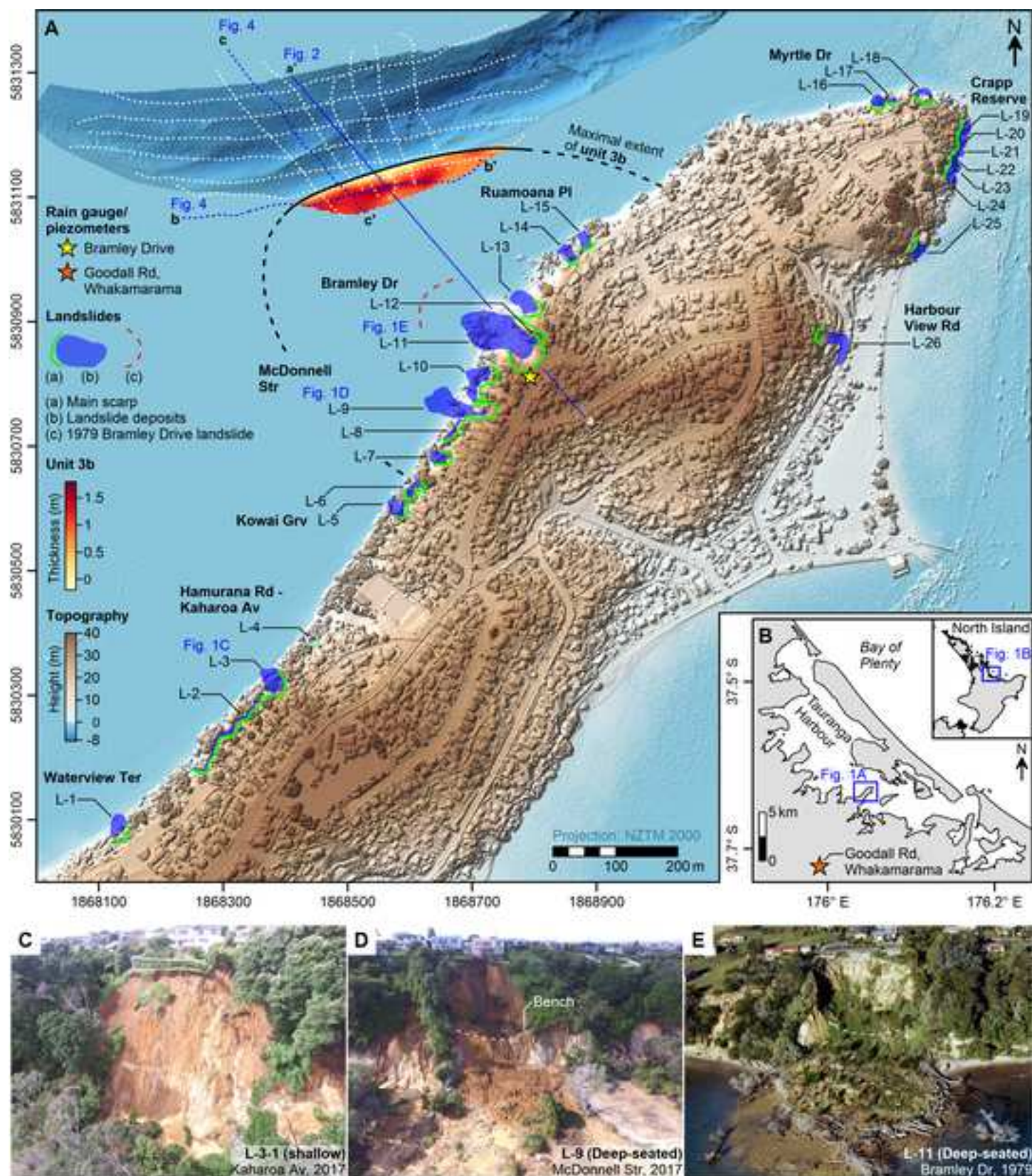
850 **Table 2.** Definitions of predictive capability variables.

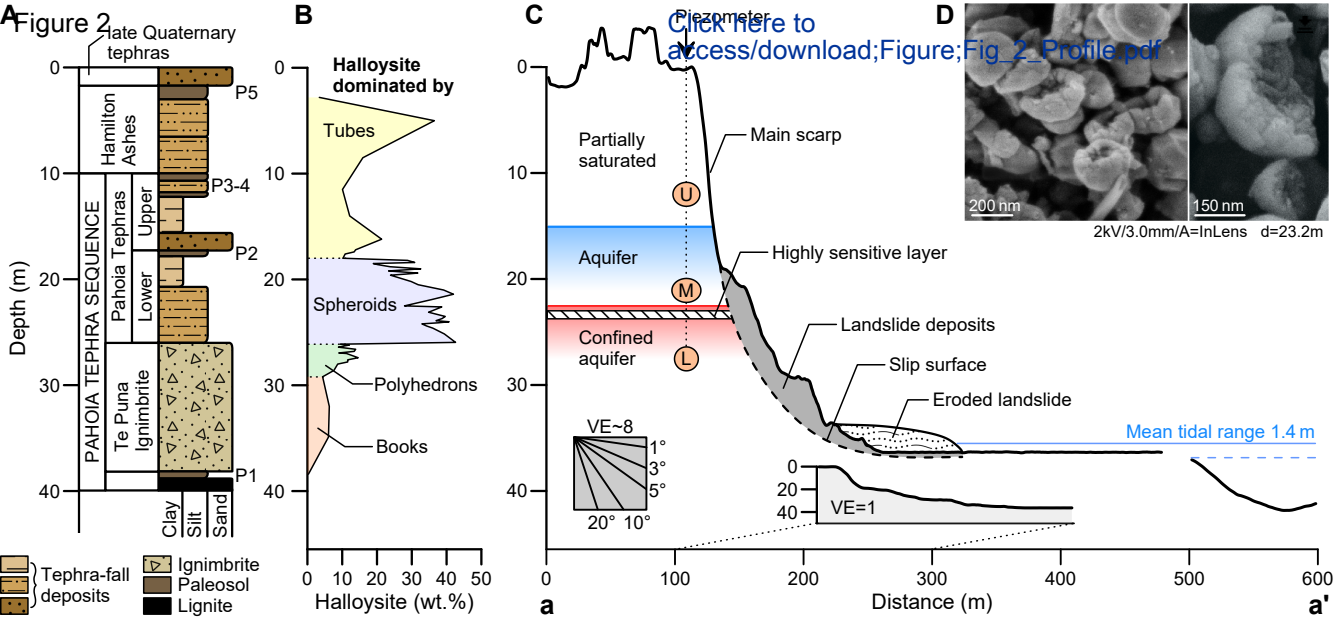
<b>Variable</b>	<b>Name</b>	<b>Description</b>
$TP$	True positives	Threshold exceeded; landslide(s)/effective stress decrease occurred
$TN$	True negatives	Threshold not exceeded; landslide(s)/effective stress decrease did not occur
$FP$	False positives	Threshold exceeded; landslide(s)/effective stress decrease did not occur
$FN$	False negatives	Threshold not exceeded; landslide(s)/effective stress decrease occurred
$Se = \frac{TP}{TP+FN}$	Sensitivity	Ability to properly classify rainfalls that caused landslide(s)/effective stress decrease
$Sp = \frac{TN}{TN+FP}$	Specificity	Ability to properly classify rainfalls that did not cause landslide(s)/effective stress decrease
$PPP = \frac{TP}{FP+TP}$	Positive prediction power	Probability of correctly classifying a rainfall that caused landslide(s)/effective stress decrease
$NPP = \frac{TN}{TN+FN}$	Negative prediction power	Probability of correctly classifying a rainfall that did not cause landslide(s)/effective stress decrease

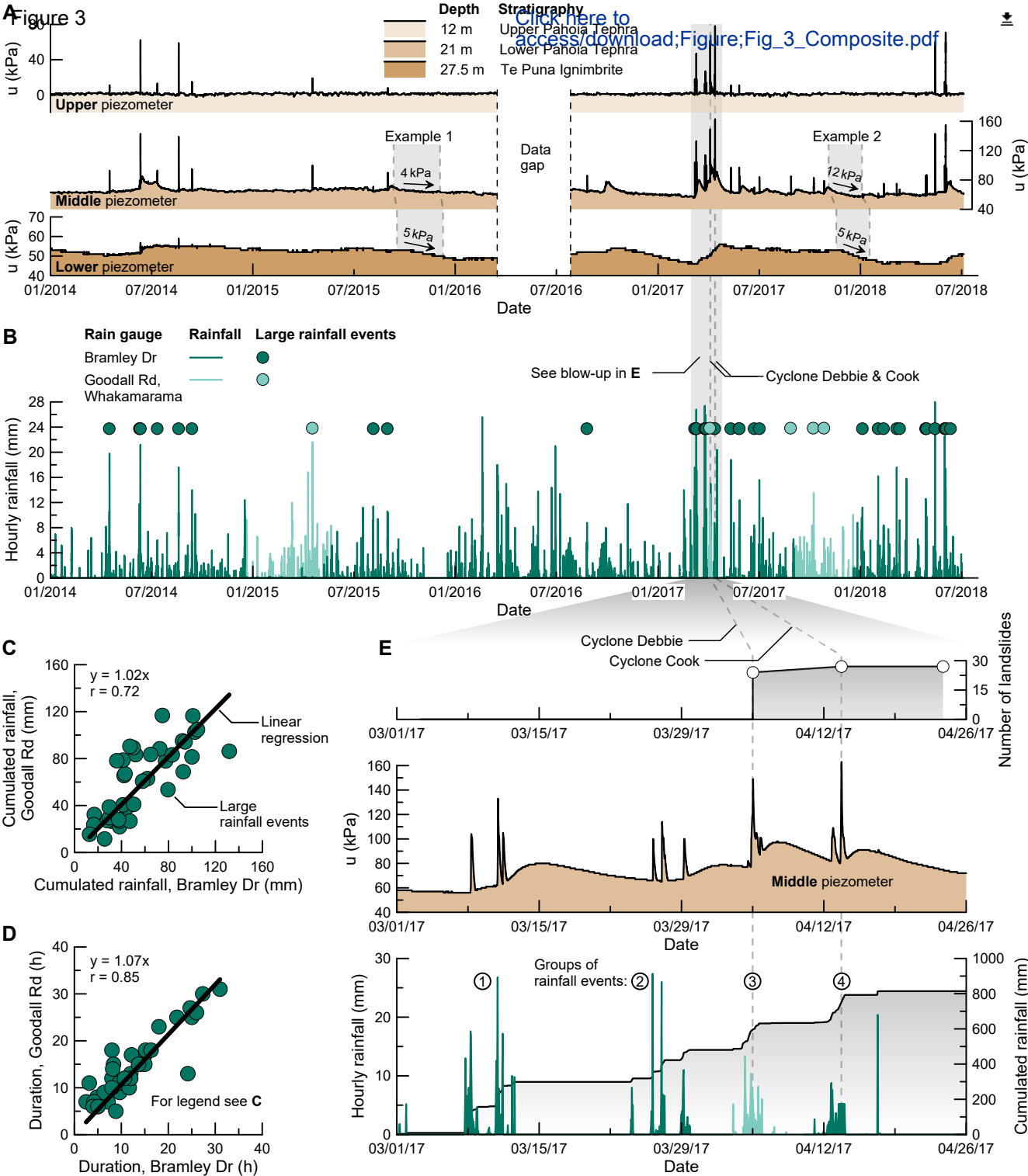
851  
852 **Table 3.** Variables\* of predictive capability for the rainfall thresholds considered in this study.

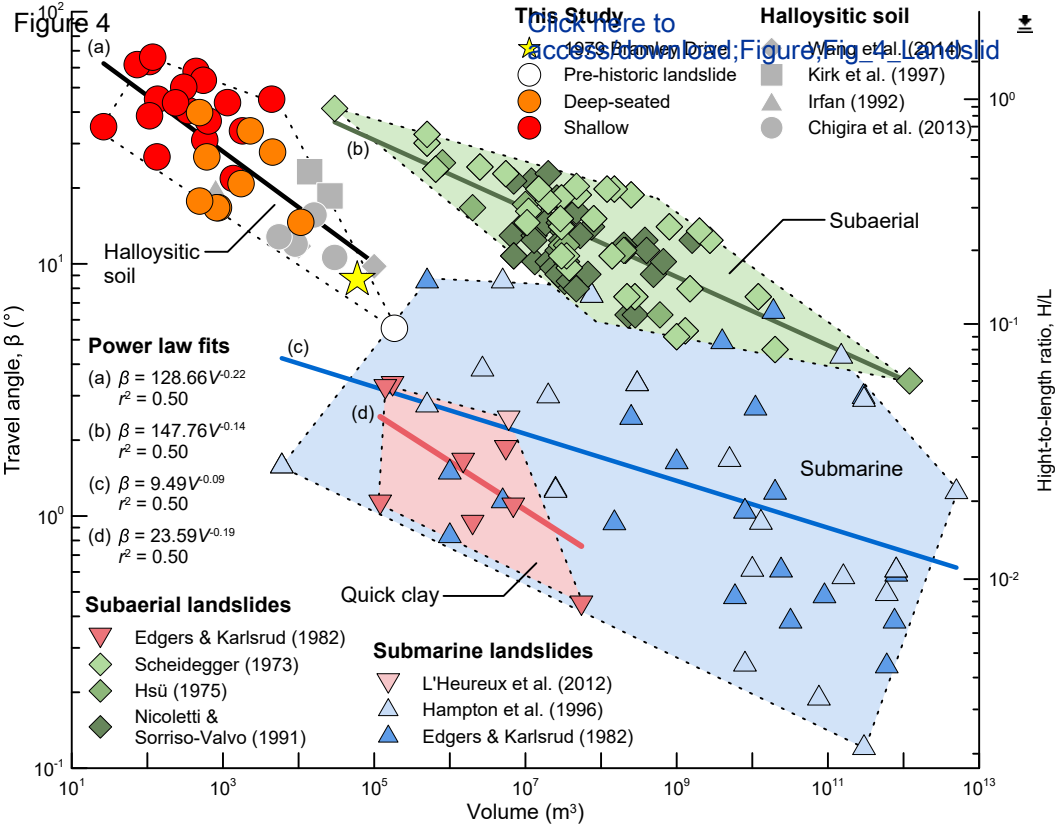
<b>Threshold</b>	<b>Aim</b>	<b>TP</b>	<b>TN</b>	<b>FP</b>	<b>FN</b>	<b>Se</b>	<b>Sp</b>	<b>PPP</b>	<b>NPP</b>
Sidle and Ochiai (2006)	Landslide occurrence	2	798	34	0	1.000	0.959	0.056	1.000
Effective stress threshold	Beginning of effective stress decrease	40	739	36	1	0.976	0.954	0.526	0.999

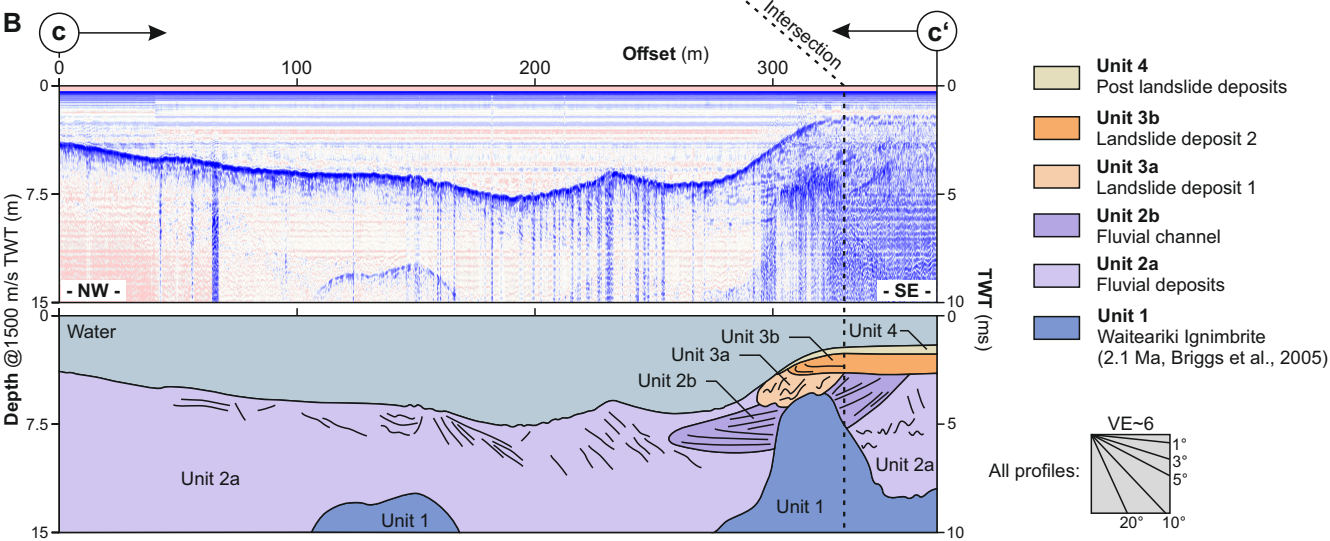
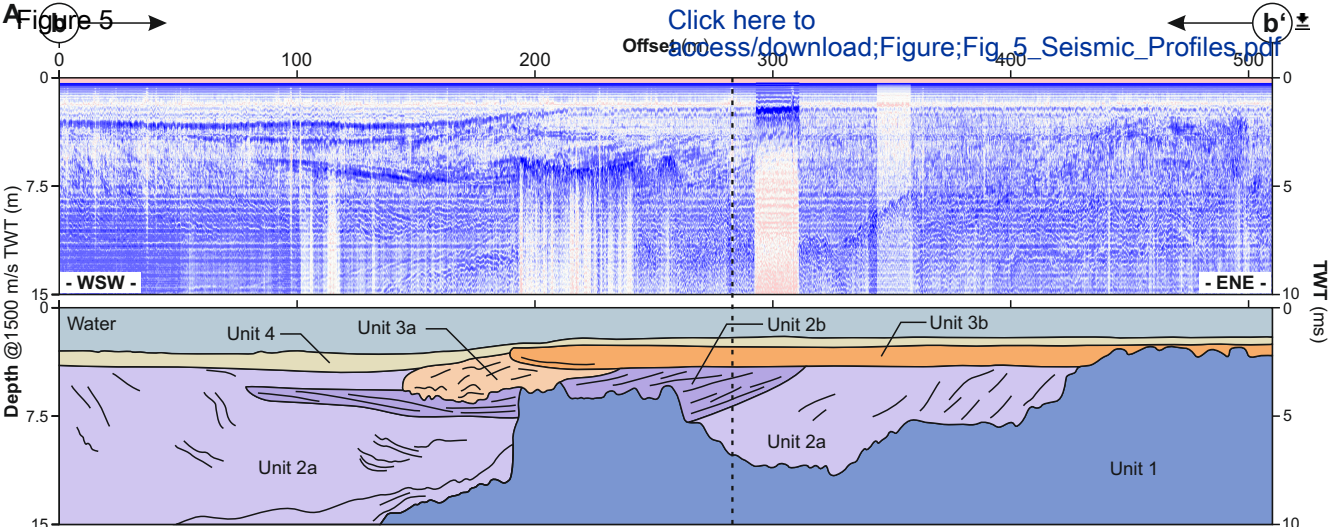
853 \*Defined in Table 2.

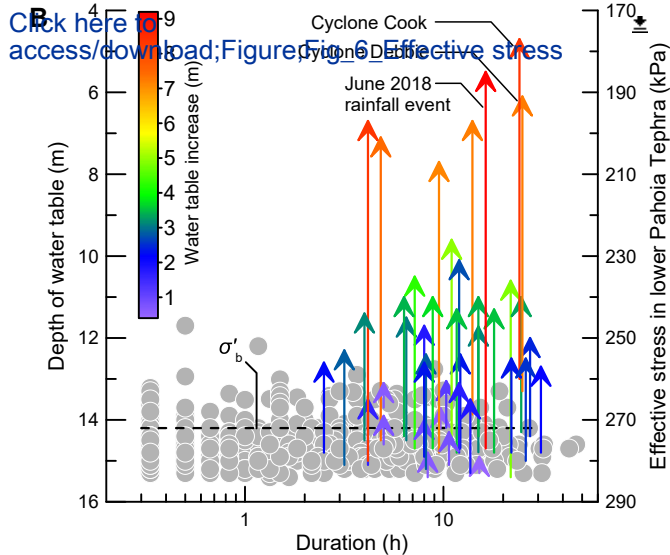
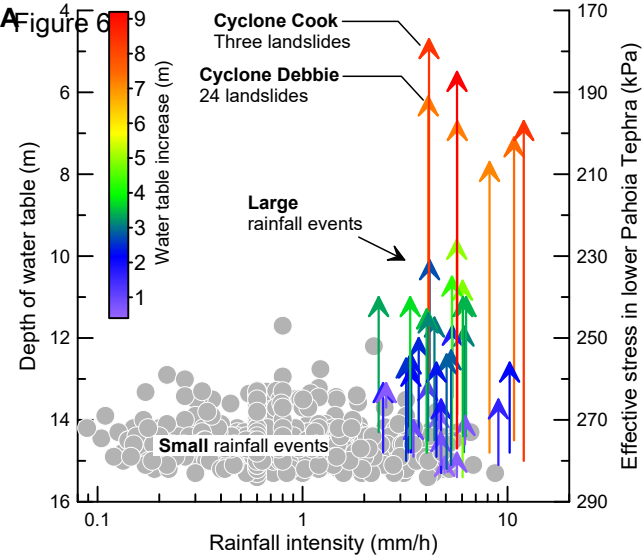












[Click here to access/download;Figure\\_Fig\\_6\\_Effective stress](#)

